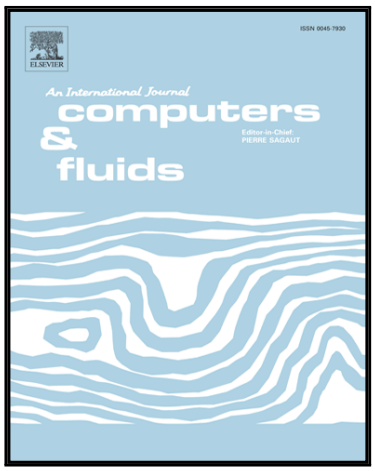

Combined Numerical and Experimental Simulations of Unsteady Ship Airwakes

Weixing Yuan , Alanna Wall , Richard Lee

PII: S0045-7930(18)30329-3
DOI: 10.1016/j.compfluid.2018.06.006
Reference: CAF 3923

To appear in: *Computers and Fluids*

Received date: 25 October 2017
Revised date: 15 May 2018
Accepted date: 11 June 2018

Please cite this article as: Weixing Yuan , Alanna Wall , Richard Lee , Combined Numerical and Experimental Simulations of Unsteady Ship Airwakes, *Computers and Fluids* (2018), doi: 10.1016/j.compfluid.2018.06.006

Highlights

- Ship airwake characteristics over the flight deck are characterized experimentally
- Computational airwake simulations are validated successfully for static frigates
- Airwake results are compared using various metrics including turbulence distributions
- Inclusion of masts plays secondary role when compared with choice of numerical scheme
- Oblique wind angles add challenges to both experimental and computational simulations

COMBINED NUMERICAL AND EXPERIMENTAL SIMULATIONS OF UNSTEADY SHIP AIRWAKES

Weixing Yuan, Alanna Wall, and Richard Lee
National Research Council (NRC) Canada, Ottawa, Ontario, K1A 0R6, Canada
Weixing.Yuan@nrc-cnrc.gc.ca

Keywords*: Unsteady aerodynamics, ship airwake, bluff-body aerodynamics, separated flow, computational fluid dynamics (CFD), detached eddy simulation (DES).*

Abstract

To aid pilot training for shipboard helicopter operations, computational fluid dynamics (CFD) is increasingly being performed to model ship airwakes. The calculated velocity field data are exported to the flight simulator as look-up tables. In the Canadian context, work to expand ship airwake simulation capabilities for future use in flight simulators is currently being done using the open-source OpenFOAM. The current paper reports on the progress of this work using the simple frigate shape 2 (SFS2), which is a highly simplified ship geometry, to validate the method for low-sea-state (also referenced to as static) cases. By employing delayed detached eddy simulations (DDES), OpenFOAM was able to compute the unsteady ship airwakes well compared to experimental data and other references. After validation, OpenFOAM was applied to the Canadian Patrol Frigate (CPF), a more representative example of a naval vessel. Hybrid structured and unstructured grids were used because of the complexity of the CPF geometry. The agreement between the computed and the experimental results for the static CPF was reasonable, which built a solid foundation supporting further development of simulation for the CPF in motion.

1 Introduction

Shipboard operations are among the most challenging of any piloting task for fixed or rotary wing aircraft [1] - [3]. The launch and recovery of helicopters is often performed from the landing decks of small ships, which are subject to pseudo-random motion in six degrees of freedom. The difficulty is increased given that the landing deck is often immersed in the unsteady ship airwake. Because of the nature of bluff-body aerodynamics, the separated flow and sheared vortices interact, resulting in a time-varying airwake with highly turbulent structures, which can significantly increase the difficulty associated with a launch and recovery manoeuvre.

As flight simulation technologies mature, simulators are being used increasingly to aid pilot training for shipboard helicopter operations. High-fidelity simulation of aircraft landing on ships offers the opportunity for trainee pilots to experience the ship environment prior to actual flight operations [3][4]. Simulation also provides a capability to test new ship and aircraft designs before building them, and has the potential to support the determination of operational limits safely without relying on the wind and weather[4][5].

A key area that affects simulation fidelity is the modelling of ship airwakes. The determination of airwake characteristics is not a trivial task, especially computationally. At-sea and wind tunnel measurements can be used to provide data from which airwake models can be generated. Although Polsky mentioned that the large scale factors required due to the available size of wind tunnels may introduce Reynolds number and frequency scaling issues when attempting to convert to full-scale values [6], the major issue with wind tunnels is that one cannot fully correlate flowfields in three dimensions since measurement techniques are usually point-wise or plane-wise. At-sea flight testing is both labour and equipment intensive, requiring a dedicated ship and potentially multiple aircraft for days at a time [7][8].

Increasingly, computational fluid dynamics (CFD) is used for modelling ship airwakes because the simulations can contain many correlated grid points. With this approach, CFD solves the flow over the ship, and for the pilot training application the resulting velocity field data are exported to a flight simulator as look-up tables. Towards this end, the CFD model must be validated against experimental or at-sea flight test data to ensure that the computed results used in the flight simulator are realistic and accurate. This was carried out using a simple frigate shape (SFS) in this study.

The simple frigate shape is a highly simplified ship geometry, which was created originally by a ship airwake modelling working group within The Technical Co-operation Program (TTCP) to provide an easily repeatable benchmark case for validating CFD codes for ship airwake applications [9]. Figure 1 shows an updated version of this configuration, the simple frigate shape 2 (SFS2), with an elongated superstructure and a pointed bow based on the original SFS. The SFS2 is a conceptual standard ship design often used to facilitate the development of CFD capabilities for ship airwakes, superseding SFS. At full scale, the SFS2 is 455 feet long (138.68 m) and 45 feet (13.72 m) wide; details of the geometry are described by Zan [10]. The SFS2 configuration has been investigated numerically by a number of researchers with commercial CFD codes. Syms [11] simulated the flow past the SFS2 configuration at model scale using the lattice-Boltzmann flow solver PowerFlow and some limited results were compared to experimental data. The renormalization group (RNG) form of the k-ε turbulence model was used. Zhang et al. [12] performed Reynolds-averaged Navier-Stokes (RANS) simulations for the SFS2 model using the commercial code Cobalt. The Spalart-Allmaras one-equation turbulence model [13] was used. Later, Zhang and Su [14] used an Euler solution to investigate the impact of the ship airwake on a Bell 412 helicopter model over the SFS2 model deck. Forrest and Owen [5] performed detached eddy simulations (DES) with the shear stress transport (SST) k-ω turbulence model [15] for flows past the SFS2 at full scale. Recently, Rajmohan et al. [16] developed a reduced order model (ROM) to study rotor/ship

aerodynamic interaction and applied the ROM formulation to the CFD flowfield inside the sampling airwake box of a scaled (130%) SFS2 model. The ROM was an ordinary differential equation approximation of the CFD governing equations that can effectively model the fundamental physical phenomena in a computationally efficient manner. In their study, the CFD simulation was performed using the open-source OpenFOAM [17], and laminar flow conditions were assumed near the ship surface.

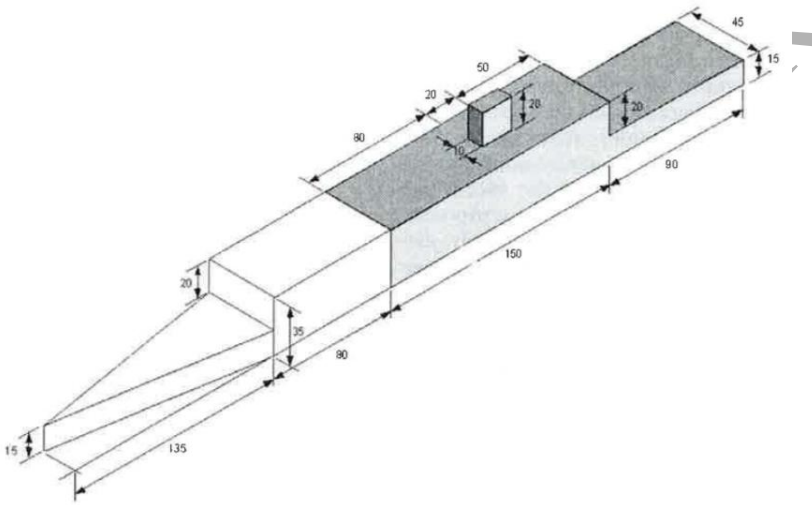

Figure 1. SFS2 configuration (original SFS shown shaded), adopted from Zan [10]; dimensions in feet.

Following the validation of the CFD approach with the SFS2 geometry, Forrest and Owen [5] applied the same methodology to a Type 23 Frigate, which is a class of warship with the UK Royal Navy. Forrest et al. [3] and Hodge et al. [8] further presented a helicopter-ship dynamic interface employing CFD data for the development of a ship airwake model. The approach to turbulence modelling used for the DES simulations was based on the Spalart-Allmaras (S-A) turbulence model [18]. Zan et al. [19] applied the commercial code CFD-ACE to a modified CPF model, where simplifications were made to the bridge and several of the small structures around the flight deck were removed. The steady-state flow simulations were performed using the k-ε turbulence model based on Launder and Spalding [20]. Generally, the Reynolds number dependence or scaling effect has not been evaluated in detail since it is assumed that the

flow over such sharp-edged bluff body structures is insensitive to Reynolds number above a lower limit. Healey proposed that a minimum Reynolds number of about 11,000 is adequate for typical ships other than aircraft carriers operating at a maximum beam-based Reynolds number of $10^7 – 10^8$ [21], assuming the flow separations occur mainly from sharp edges.

In Canada, the ship airwake simulation capabilities are being expanded to include ship motion. OpenFOAM, an open-source CFD software, is being evaluated for its suitability for studies involving ship motion and as the means for the expansion of Canada's simulation capabilities. OpenFOAM was selected for its cost effectiveness because it obviates the cost and restrictions which CFD users encounter with commercial CFD software licenses. OpenFOAM is flexible: it provides a large selection of numerical schemes and parameter setups; its solid-body motion solver can be applied to one degree-of-freedom (DOF) motions; and OpenFOAM has motion solvers and libraries for simulations with dynamic meshes for specific conditions and applications. These dynamic mesh functions, however, require further development and validation for complex ship motion, such as two- and multi-DOF rigid-body motion. While the use is free and OpenFOAM is attractive, there are offsetting drawbacks. Technical support for OpenFOAM is not free and can be costly. Development is difficult, even though free access to the source code provides flexibility and makes development task feasible. Extensive CFD experience is required to ease the cost of technical support and development.

To adapt OpenFOAM further for ship motion, the solid-body and dynamic-mesh solvers require modifications. In Canada, a mesh morphing functionality is being incorporated. The mesh morphing function is based on radial basis function (RBF) which handles the motion of the ship with a deforming free-surface boundary. NRC has been successful in the past with applying the RBFs to aeroelastic simulations [22].

Although the solver and control parameters differ between the static and motion cases, the procedure for executing the two types of simulation is similar. With regards to performance, the computations for the motion cases are about 50% slower than the static cases, depending on the motion profile. The preliminary results for unsteady airwakes behind ships in motion, using the aforementioned solid-body and/or dynamic RBF solvers, are reported in Ref. [23]. The simulations for low-sea states cannot capture the effects resulted from or related to ship motions. Although ship motion effects on airwake could play an important role when large amplitude ship motions are present, as pointed out by Zan [10], the topic of high-sea states with large-amplitude ship motion is beyond the scope of this paper.

This paper reports on the progress of applying OpenFOAM to the simulation of ship airwakes in low-sea states, first with the SFS2 to validate the static cases, that is, cases where the ship is not in motion, and then to the more complex geometry of the Canadian Patrol Frigate (CPF). The data set created for the CPF is used to produce flight simulator look-up tables. Preliminary results of this work have also been presented in Ref. [24]. This work is a promising step towards realistic engineering applications, in which flowfields around a ship geometry – at the same level of complexity as a real-world frigate – are simulated with in-house computational and experimental means. In addition to supporting flight simulators, the capability to develop high-quality simulations of ship airwake is applicable to the design and development of ships, the clearance and qualification of maritime helicopters to land onto and take-off from ships, and the selection of the appropriate placement of the ship anemometer. The requirements for each of these applications are subtly different, depending on the goals of the work; for instance, as discussed later in the paper, including ship anemometer masts in the computations for flight simulation development is not as crucial as evaluating the placement of these anemometers on the ship.

2 Computational and Experimental Setups for the SFS2

As part of the development of the SFS2, the airwake over the flight deck was characterized experimentally in the NRC 2 m × 3 m wind tunnel. The wind tunnel is a well-credited facility for subsonic aeronautical and industrial testing [25]. The test section of the wind tunnel is 1.9 m × 2.7 m × 5.2 m. Maximum speed can reach 140 m/s with a turbulence level of 0.14%. In this study, a hot-film survey was carried out over the flight deck behind a 1:100 scale model of the SFS2 geometry, as shown in Figure 2. In naval terminology, winds from starboard are denoted as "Green" and winds from port as "Red". In this study, a hot-film survey was carried out for the flight deck for a headwind and a Green 45° wind condition. The velocities are expressed in ship axes, where the origin of the body-axis coordinate system lies on the centreline of the flight deck at the intersection of the flight deck surface and the aft face of the hangar, as shown in Figure 2. The survey grid over the flight deck is termed Map 1 for the headwind case and Map 3 for the Green 45° wind condition. In addition, a hot-film survey was conducted around the superstructure for a headwind, a Green 45° and a Green 90° wind condition. Details are available within the TTCP community (Lee, R. SFS 2 Code Validation Data Update. 2003).

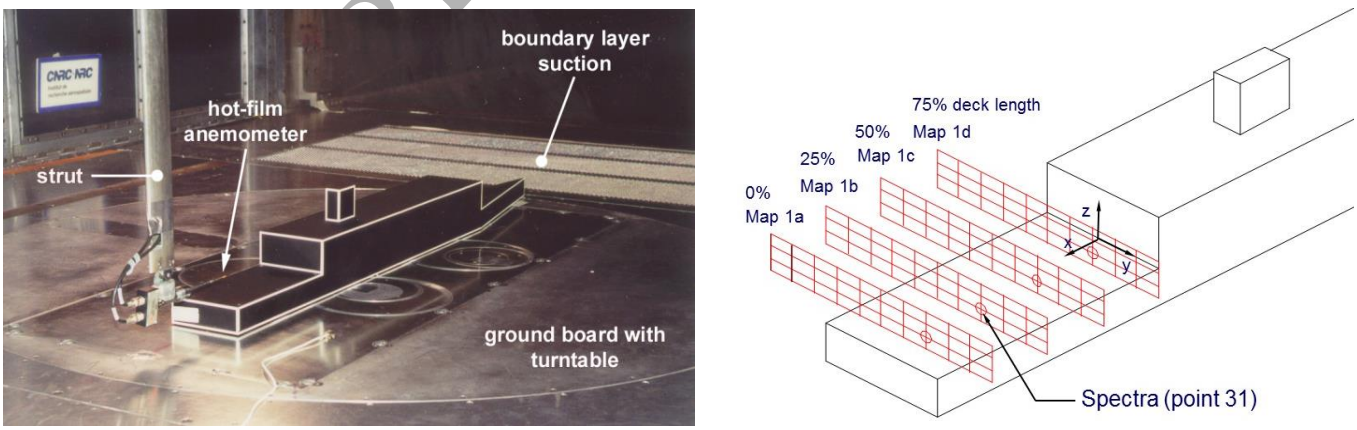

Figure 2. SFS2 model mounted inside the NRC 2 m × 3 m wind tunnel and the hot-wire survey grid over the flight deck of the SFS2 model.

To develop confidence with OpenFOAM, computations were first performed for the SFS2 model. The purpose of this work was to validate the results produced by OpenFOAM [26] against experimental data and to determine whether OpenFOAM is suitable for ship airwake simulations. OpenFOAM was applied to compute the three-dimensional (3D) unsteady incompressible flows over the SFS2. The OpenFOAM pressure-based Navier-Stokes solver, Pimple, was used in this study. OpenFOAM applies the integral form of the conservation laws of mass and momentum on an unstructured grid. A fully-implicit, second-order temporal differencing scheme was implemented in the discretization. The discretization of the convective and diffusive fluxes was carried out in a co-located variable arrangement using a finite-volume approach, which was second-order accurate in space. The coupling of the pressure and velocity was handled using a modified SIMPLE algorithm in the Pimple computations. Because of the nature of the bluff-body aerodynamics, the Spalart-Allmaras delayed detached eddy simulation (DDES) was employed to model the turbulence [27].

A C-H type structured grid was used in this study. The computational domain is shown in Figure 3. The farfield of the computational domain was set at $5l_s$ and the depth of the domain was set to $0.75l_s$, where l_s represents the total length of the ship. These parameters are comparable to or slightly larger than the values used by Forrest and Owen [5] for their cylindrical mesh. Although OpenFOAM is designed for unstructured grids, a structured grid was used because the geometry of SFS2 is not complex. The structured grid helped reduce the amount of mesh cells and improved the quality of the grid. The outer farfield boundary was set as an inlet or outlet, depending on the local flow direction. Both upper and lower surfaces were set as slip boundary conditions. The ship surface was modeled as a wall with a no-slip boundary condition.

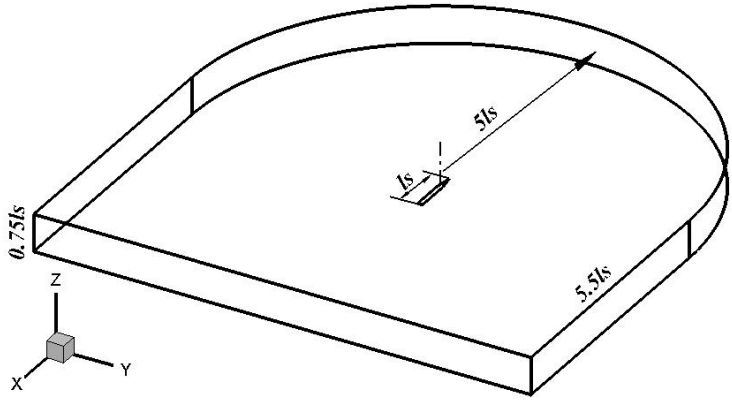

Figure 3. SFS2 computational domain.

Forrest and Owen [5] have carried out grid convergence studies for the SFS2 geometry. They chose a baseline spacing (Δ_0) and scaled this up and down by a factor of $\sqrt{2}$. The test computations were performed for a headwind at a freestream speed of 40 knots (20.58 m/s), and the grids had 10.4×10^6, 5.8×10^6, and 3.3×10^6 cells, for spacings of $\Delta_0/h = 4.12\times10^{-2}$, 5.83×10^{-2}, and 8.33×10^{-2}, respectively, where h is the hangar height. When comparing mean flow velocities and turbulence intensities over the flight deck, little difference was found between the results obtained based on the three meshes, indicating grid-independent solutions. Considering the requirements for the appropriate level of frequency of wake flow and their computational resources, they decided to use the medium mesh for their computations. Forrest and Owen's grid convergence studies were used as guidelines to generate a grid in this study. In the present work, a block-structured mesh was generated. The spacing in the ship airwake was one foot at full scale in all three directions, which corresponds to a spacing of $\Delta_0/h = 0.05$, and the mesh had about six million cells, slightly finer than Forrest and Owen's medium grid. The maximum spacing normal to the wall gave averaged wall unit values of $y^+ \sim 65$, which is similar to Forrest and Owen's $y^+ = O(10)$. This number is significantly higher than the conventional requirement ($y^+ \sim 1$) for attached flows. However, this maximum was located at the end of the bow where flow accelerates, and therefore is believed not to impair the characteristics of the ship airwake. As will be confirmed later, this did not adversely affect the

accuracy of the results because the ship airwake flow is mainly inertia-driven and the separation points are fixed by the sharp edges rather than caused by boundary layer separation.

As Zan [28] pointed out, reasonable agreement between CFD and experiment at one wind angle cannot be considered as a complete validation for a CFD approach. In this study, computations were performed for a headwind and a Green 45° wind condition, and compared directly with the results from the corresponding wind tunnel study. To be consistent with the wind tunnel experiments, the freestream velocity U_∞ was set to 60 m/s for the headwind case, and 50 m/s for the Green 45° wind condition. The computations were started from a static uniform flow set as freestream. In the wind tunnel study, data were collected at a frequency of 2,000 Hz, which corresponds to a timestep (Δt) of 5×10^{-4} seconds. Based on the non-dimensional timestep employed by Forrest and Owen [5] for their full-scale simulations, a timestep of 4×10^{-5} seconds was used in the current work. The computations were started using this nominal timestep for the headwind case. The resulting non-dimensional timesteps, Courant–Friedrichs–Lewy (CFL) numbers, were $CFL_{mean} = 0.1$ and $CFL_{max} = 40$ for the headwind case and $CFL_{mean} = 0.07$ and $CFL_{max} = 200$ for Green 45° wind condition, respectively, with CFL_{max} at the pointed bow and CFL ~ 1 in the airwake, see Figure 4. Further tests showed that the timestep could reach 1×10^{-4} seconds without encountering numerical instabilities while delivering reasonable results. To ensure consistency, all results reported in this paper were obtained using the nominal timestep, unless stated otherwise. The computations were performed for eight seconds of physical time, resulting in 346 units of flow through time (l_s/U_∞), with 330 used for the final spectral analysis.

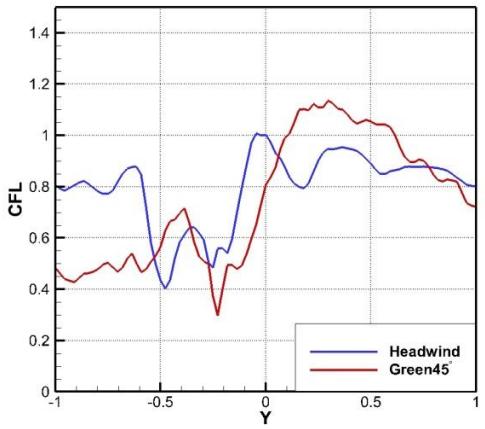

Figure 4. CFL number distribution at 50% deck length (Maps 1c for headwind and 3c for Green 45° wind) for the SFS2 model, plotted at hangar height. The lateral position is normalized by the ship beam *b*.

In this study, ten pressure and velocity coupling Pimple iterations were performed per timestep as a standard. Increasing the number of iterations to 50 did not improve the accuracy of the solution. To accelerate the computations, the computational domain was decomposed into 64 blocks for parallel computations.

3 SFS2 Results and Discussion

3.1 Mean Velocity

To be consistent with the experiments, the velocities are expressed in body axes using the body-axis coordinate system shown in Figure 2. Figure 5 depicts mean velocity along a lateral plane located on Map 1c for the headwind case and Map 3c for the Green 45° wind condition. The plane is located at 50% of the flight deck length. Laterally, the plane spans two beam widths, symmetrically about the centerline of the ship. Vertically, the plane's total height corresponds to 75% of the hangar height and its elevation above (distance from) the flight deck is 50% of the hangar height. This location represents a spot at which a helicopter would be hovering during a landing maneuver. The computed results are comparable to the

work of Forrest and Owen [5]. For comparison, their results are also plotted in Figure 5 (labelled as "Liverpool").

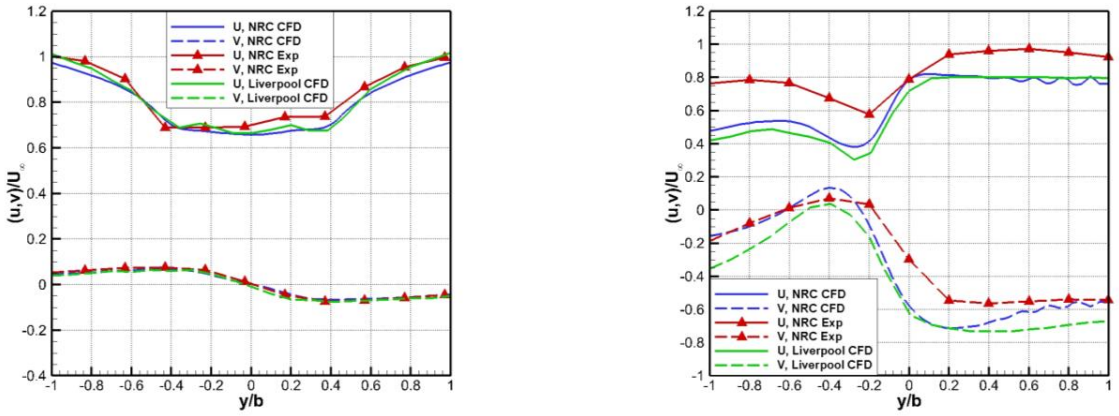

Headwind, Map 1c Green 45° wind, Map 3c

Figure 5. Mean velocity magnitudes normalized by freestream velocity U_∞ at 50% deck length (Maps 1c and 3c), plotted at hangar height. The lateral position is normalized by the ship beam *b*.

For the headwind case, a reduction in longitudinal velocity can be seen near the centre, within the wake behind the hangar. Significant gradients exist in the time-averaged values of the velocity components, which are believed to affect the trim of the helicopter. Despite the symmetric velocity distributions from CFD compared with the slightly asymmetric velocity distribution in the experiments, all of the trends measured in the wind tunnel data are generally replicated by the CFD. The maximum discrepancy of the mean velocity between the current CFD and the experimental results is approximately 3%, which represents excellent agreement.

The computations for the Green 45° wind condition were more challenging. At Green 45° wind condition, the flow over the flight deck is dominated by separated flows from the windward vertical edge of the hangar and the windward deck edge, and a vortical structure formed at the corner of the windward edge of the hangar roof. Compared with the headwind case, the separated off-body flow region is larger and more complex. A comparison between CFD and wind tunnel results for the Green 45° wind condition

shows that the velocity distribution trends were qualitatively captured by the CFD. There are obvious differences in the longitudinal and lateral components of velocity; however, these differences are comparable to the results reported by Syms [11] and Forrest and Owen [5]. The results from the present study agree well with those of Forrest and Owen, and the agreement with the wind tunnel results is slightly better. In the latter case, the better agreement is attributed to the fully structured grid used in the current study, as opposed to the unstructured grid employed in the work of Forrest and Owen.

Forrest and Owen have suggested that the discrepancies may be attributed to a difference in the incident flow between the CFD and the experiment [5]. The incident flow in the wind tunnel was believed to be aligned approximately 5° closer to the ship centreline than in the CFD calculations. A further investigation with parametric CFD studies was proposed to investigate this hypothesis [24]. To obtain deeper insights into the aforementioned discrepancies between CFD and the experiment, additional simulations for Green 40° and 35° wind conditions were carried out. Figure 6 shows a lateral plane located on Map 3c for the Green 45°, 40° and 35° wind conditions with the experimental data at Green 45° wind condition. When compared with data obtained at Green 45° wind conditions, the predicted longitudinal velocities for Green 35° and 40° wind conditions are closer to the experimental data at Green 45° wind condition. However, discrepancies are still obvious. Moreover, the comparison of the lateral velocities is unsatisfactory, in particular on the portside. This exercise concludes that the flow incident did not play a key role in causing the discrepancies. Combined with a cross-check with the experimental documents, it is believed that the discrepancies are due to “shadowing” of the cross hot-film anemometer (one film is in the wake of the other) at this wind direction. The cross hot-film anemometer was not calibrated for this situation.

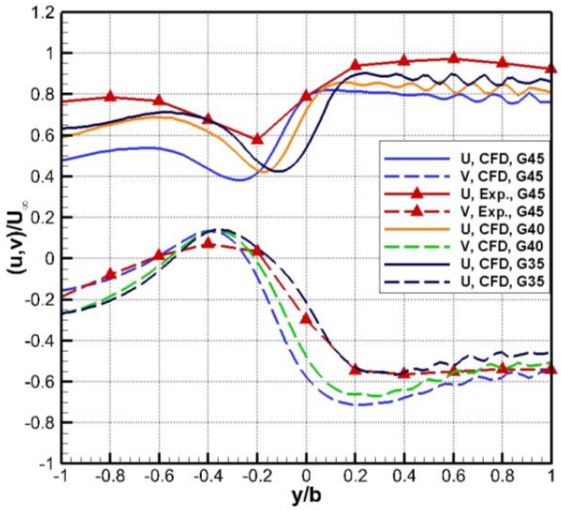

Figure 6. Effects of flow incidence on mean velocity magnitudes, normalized by freestream velocity U_∞ at 50% deck length (Map 3c) and plotted at hangar height. The lateral position is normalized by the ship beam *b*.

Figure 7 illustrates the time-averaged longitudinal and lateral velocity distributions from the hot-film survey and the computations on the four airwake planes over the flight deck for both the headwind and Green 45° wind conditions. While the hot-film probe has good resolution and fast response, it cannot differentiate between forward and reversing flows. Thus, experimental data in reverse flows are unreliable and are not shown in the figure. The data were non-dimensionalized by the freestream speed. The flow pattern at the headwind condition shows excellent agreement between the CFD and experimental results. A classic bluff-body wake arises, in which a significant momentum deficit is observed above the flight deck. For the Green 45° wind condition, the CFD results show the correct trend in the flow pattern, in particular for the lateral velocity, with some differences for the longitudinal velocity when compared with the experimental data.

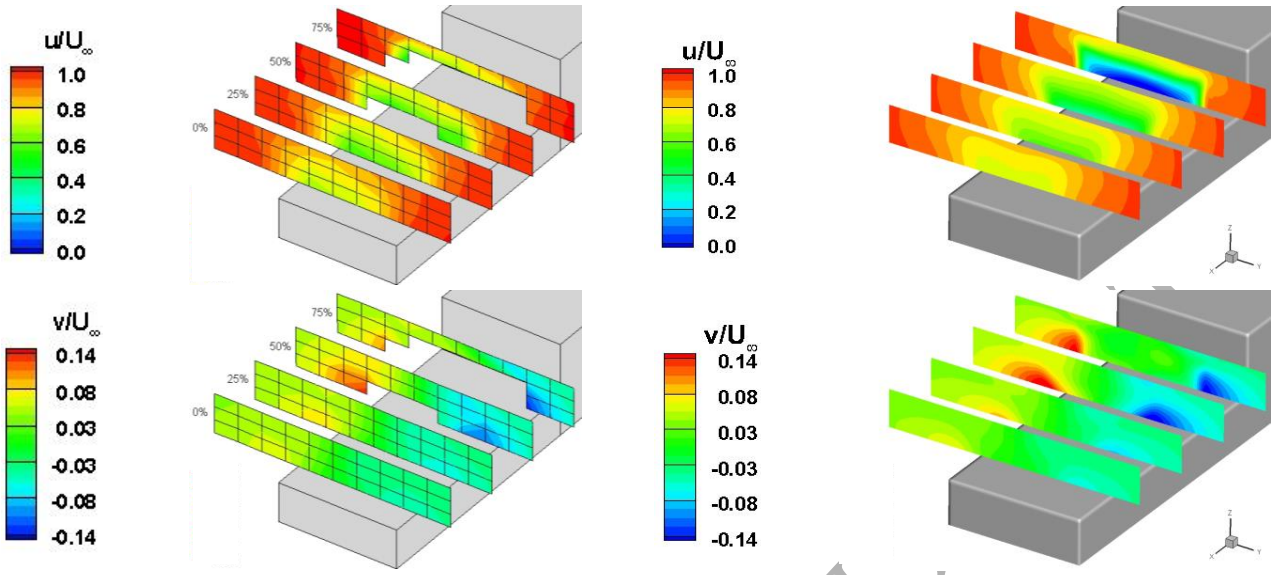

Headwind, Exp. Headwind, CFD

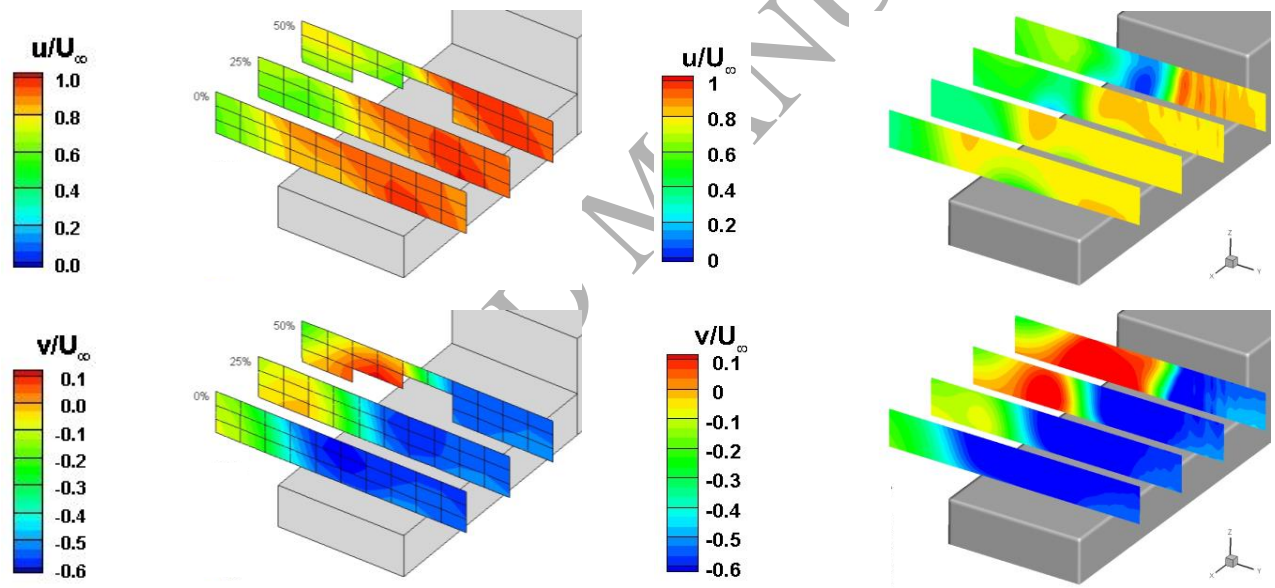

Green 45° wind, Exp. Green 45° wind, CFD

Figure 7. Mean velocity contours on off-body planes over the flight deck (Maps 1 and 3). The velocity is normalized by the freestream velocity.

3.2 Turbulence Intensity

Figure 8 shows the computed turbulence intensities compared with the wind tunnel data. In general, the present CFD slightly under-predicted the x-component and over-predicted the lateral one. As with the mean velocities, the computations are in better agreement with the experimental data for the headwind case when compared with the Green 45° wind condition. This is attributed to the latter case having more complex flow physics. Although they did not match exactly in magnitude, the CFD and wind tunnel data featured consistent trends. As shown in the figure, the levels of turbulence increase as the flight deck is approached laterally. The increased turbulence will contribute to pilot workload through the requirement to respond to predict disturbances, mainly in the frequency range of 0.2 – 2 Hz [29]. Pilot workload is also affected by other factors, including control units and cueing.

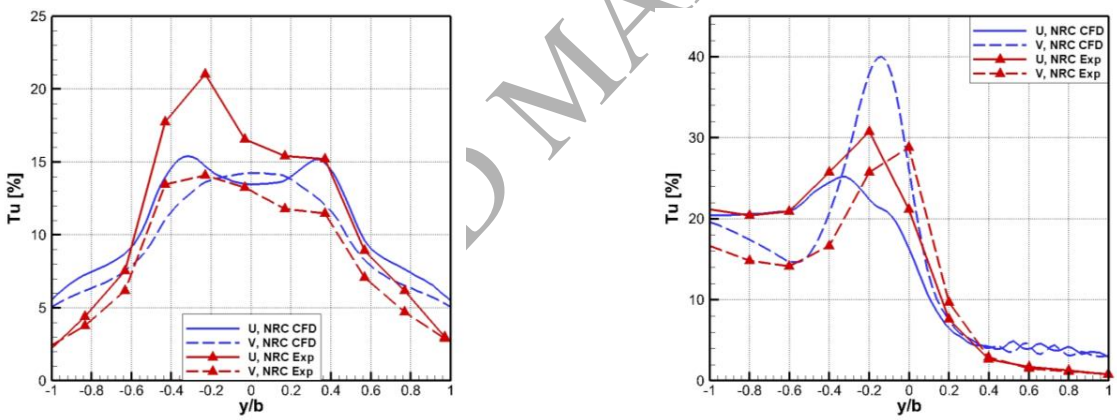

Headwind, Map 1c Green 45° wind, Map 3c

Figure 8. Turbulence intensities normalized by U_∞ at 50% deck length (Maps 1c and 3c), plotted at hangar height. The lateral position is normalized by the ship beam *b*.

3.3 Spectral Characteristics

Figure 9 shows plots of power spectral density, where the velocity data have been recorded at point 31 located near the end of the flight deck on Map 1c for the headwind case and Map 3b for Green 45° wind condition as shown in Figure 2. For both CFD and the experiments, the spectral characteristics were developed from time-series data, employing a Fourier transform algorithm within a 1,024-sample window.

The experimental velocity spectra represent an average of three runs; the sampling duration of each run was 16.4 seconds. The CFD simulations, however, were performed for a physical duration of eight seconds; as a result, the CFD results exhibit more scatter. Nonetheless, the agreement between CFD and wind tunnel data is promising, both in terms of frequency content and power.

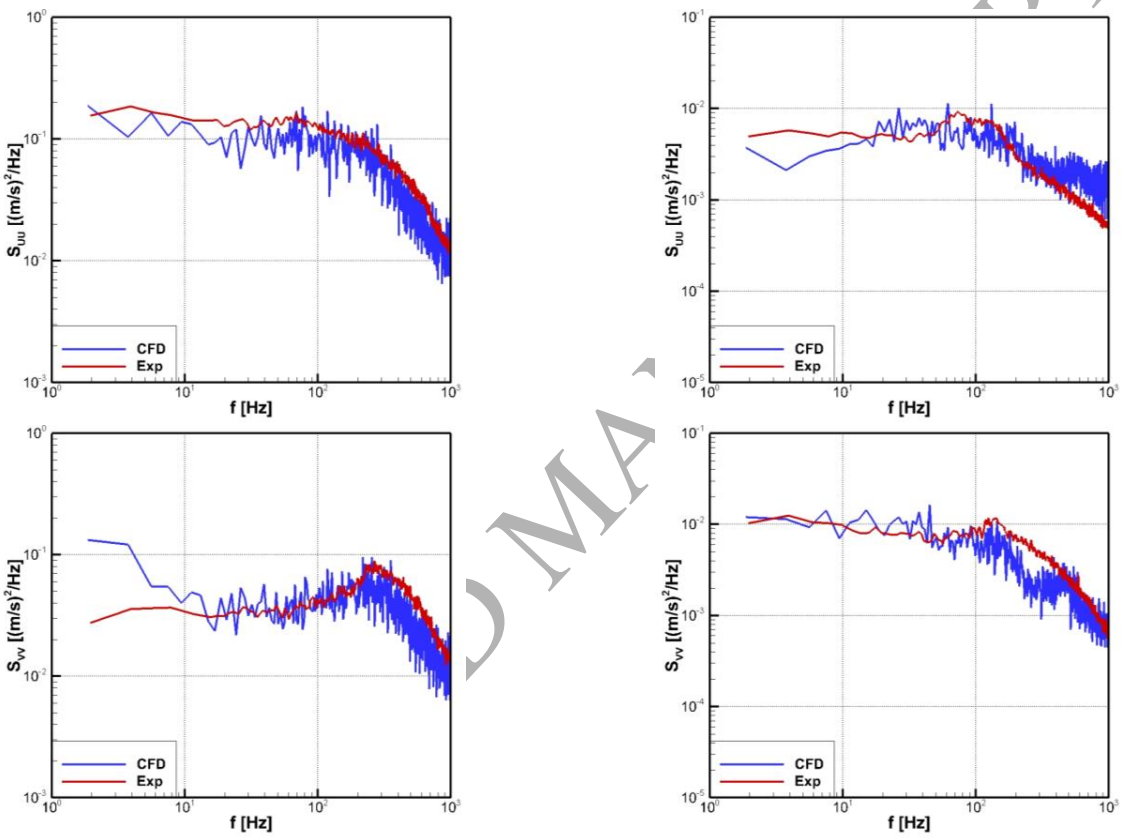

Headwind Green 45° wind

Figure 9. Power spectral density plots of longitudinal and lateral velocity components recorded at point 31 on Map 1c for headwind and Map 3b for Green 45° wind conditions.

3.4 Pressure Distributions

Computational fluid dynamics has the advantage of acquiring data from a number of sample points simultaneously, allowing the computation of mean values and spatial correlations for both velocities and pressure. Although pressure data are not used as input for flight simulators, from a research perspective, the pressure field helps with the understanding of the flow physics. Figure 10 to Figure 12 illustrate the pressure distributions on the frigate surface and surrounding areas. The figures clearly show low- and high-pressure regions, reflecting separated flow, impingement and reattachment areas. Compared with the headwind case, the pressure field at the Green 45° wind condition is more complex. The flow showed full three-dimensionality at both angles. Pressure data were not acquired experimentally.

Headwind Green 45° wind

Figure 10. Mean pressure coefficient distribution on SFS 2 surfaces.

Headwind Green 45° wind

Figure 11. Mean pressure coefficient distribution on the mid plane at Y = 0.

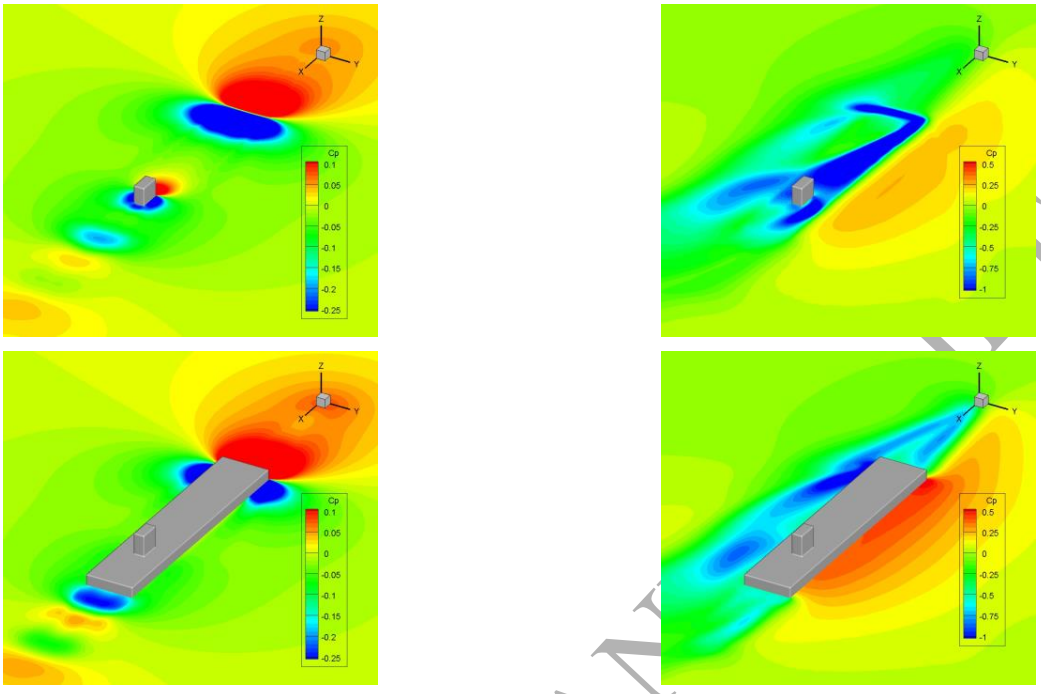

Headwind Green 45° wind

Figure 12. Mean pressure coefficient distribution on planes at *Z/h* = 0.5 (lower) and 1.5 (upper). The vertical position is normalized by the ship hangar height *h*.

3.5 Freestream Turbulence Effects

When using the DDES model, the eddy viscosity ν_t and its model parameter $\tilde{\nu}$ need to be set at the freestream. Available real values from measurements are ideal for the use in CFD studies. As the parameters are unavailable, in the present study, $\tilde{\nu}$ and ν_t were both set to 100ν, where ν is the laminar viscosity. This setup provided the best results when compared with the measured ship airwakes. Conventionally, turbulence is characterized by intensities and length scales. Similar to Ref. [30], the wind tunnel values in the freestream were calculated as follows:

$$\nu_t = \sqrt{3/2}\, C_\mu\, Tu\, L\, U_\infty, \tag{1}$$

where *Tu* represents turbulence intensity, *L* is the turbulence length scale, and U_∞ is the freestream speed. The constant C_μ is 0.09. Since the turbulence intensity of the wind tunnel is known ($Tu = 0.14\%$), but the turbulence length scale is not, the turbulence length scale *L* was varied to define the turbulence viscosities in the freestream. There were marginal differences in the results for the headwind case. Figure 13 shows two sets of results from computations using Δt =1×10^{-4} seconds at the Green 45° wind condition with assumptions of *L* = 0.043*b* and 4.3*b*, where *b* is the ship beam. The resulting turbulence viscosities were ν_t = 3ν and 300ν, respectively. Although the different parameters did not change the mean velocity distribution (as in Figure 5), the spectral characteristics were affected, both in terms of frequency content and power. Having accurate freestream turbulence characteristics for the wind tunnel would help define the effective turbulence viscosity and thus improve the numerical results.

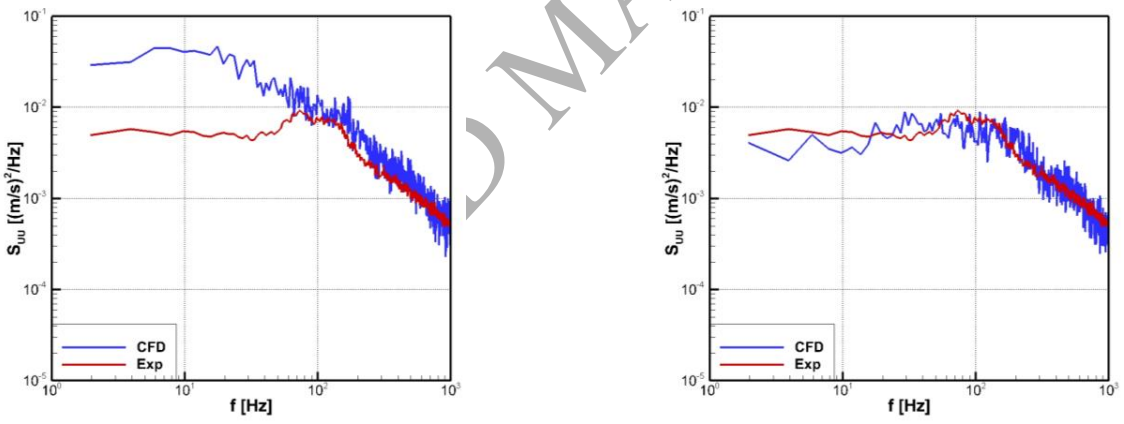

$Tu = 0.14\%, L = 0.043b, \nu_t = 3\nu$ $Tu = 0.14\%, L = 4.3b, \nu_t = 300\nu$

Figure 13. Freestream turbulence length scale effects for Green 45° wind condition, at point 31 on Map 3b. Turbulence viscosity at freestream is defined by $\nu_t = \sqrt{3/2} C_\mu TuLU_\infty$.

3.6 Reynolds-number Effects

The aforementioned validations were carried out based on simulations for the SFS2 configuration at model scale. The Reynolds numbers based on the freestream and the beam length were 5.4×10^5 for head wind and 4.5×10^5 for Green 45° wind conditions. Although the geometries were similar at both the full

scale and model scale, not all dynamic similarities were retained. One important dynamic similarity is the Reynolds number. Normally, it is assumed that the flow over bluff-body structures, like the ones discussed in this paper, is insensitive to Reynolds number above a certain limit, and the flow topology at model scale should be replicated at full scale. The limit for Reynolds number sensitivity can be geometry dependent. As Polsky [6] pointed out, this has not been shown conclusively, and the question of scale is never far from the forefront. Forrest and Owen [5] investigated Reynolds number dependence, but only for the headwind condition. To confirm the insensitivity or independency, in the present study, additional simulations were performed for the SFS2 geometry at full scale. The freestream was assumed to be 20 m/s, equivalent to a Reynolds number of 1.8×10^7. Figure 14 and Figure 15 compare the computed results at model and full scales. In Figure 15, the experimental and CFD data at model scale have been scaled using the reduced frequency to match the full-scale CFD conditions. As can be seen from the figures, marginal discrepancies are evident for the mean velocities and turbulence intensities. The spectral densities showed good agreement. As the spectral density was averaged based on 191,000 sampling timesteps at model scale, while only 23,000 timesteps were sampled at full scale, the spectral density showed more scatter at full scale. Nevertheless, the frequency content and power for the full scale are the same as for the model scale. This exercise confirmed numerically the insensitivity of the flow to Reynolds number for the bluff-body geometries currently investigated.

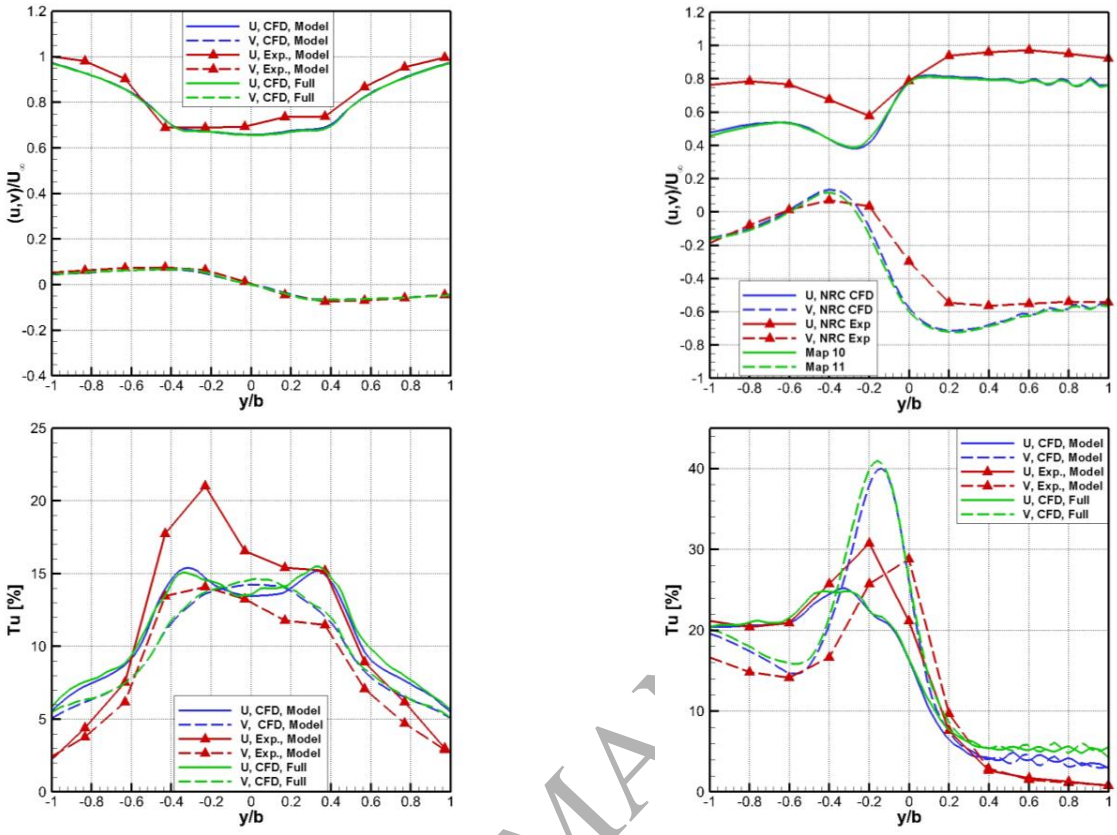

Headwind, Map 1c

Green 45° wind, Map 3c

Figure 14. Comparisons of computed results at model and full scales: Mean velocity magnitudes and turbulence intensities normalized by freestream velocity U_∞ at 50% deck length (Maps 1c and 3c), plotted at hangar height. The lateral position is normalized by the ship beam *b*.

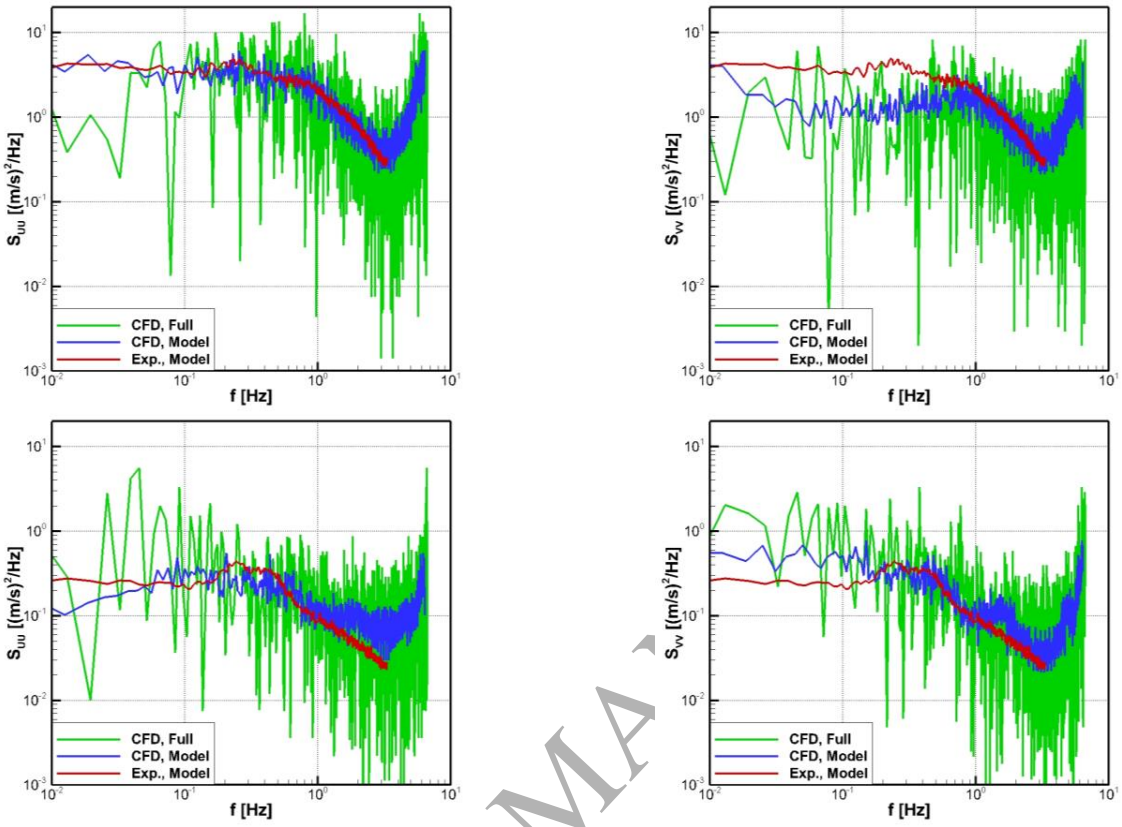

Headwind Green 45° wind

Figure 15. Comparisons of computed results at model and full scales: Power spectral density plots of longitudinal and lateral velocity components recorded at point 31 on Map 1c for headwind and Map 3b for Green 45° wind.

4 Computational and Experimental Setups for the CPF

4.1 Cobra Probe Measurements

The NRC has been supporting various aspects of helicopter operation in the airwake of the CPF for many years. Some data collected under previous experimental campaigns were used as validation data for this project. The first set of complementary experimental data is a set of three-point three-dimensional, high-speed flow measurements at various wind directions. These data are relevant for validating three-dimensional flow mean and unsteady components, as well as spectra at the three measured points in the airwake. These experiments were conducted at the NRC 3 m × 6 m wind tunnel [31] in 2013 and have not

previously been published in the public domain. For this test, the test section of this open-circuit wind tunnel was set to a half-insert configuration that was 3.1 m wide, 5.4 m high and 6.4 m long. The experiments were conducted using the electric drive for the wind tunnel fan, which can generate nominal speeds of up to 44 m/s in the test section with inserts.

Triangular spires were used at the entrance of the test section to produce a representative atmospheric boundary layer. The boundary layer approximates the typical characteristics given in Ref. [32] with a power law exponent close to 0.14 for a reference height of 19.5 m. A 1:50-scale CPF model was used for this study. A nominal reference wind speed of 20 m/s (40 kts) was chosen for this airwake study because this speed corresponds to a mid-range wind speed for helicopter operations, if a velocity scale of 1:1 is employed. To capture any Reynolds number effects that might be at play in this set of tests, reference wind speeds of 10 m/s (20 kts) and 30 m/s (60 kts) were also tested; the results were determined to be insensitive to Reynolds number within the accuracy of the test results.

Three points in the airwake (located starboard, port, and at mid deck in the CPF airwake, at a height and longitudinal location close to the rotor disc in high hover), were setup for velocity measurements using Cobra probes (Figure 16). Developed by Turbulent Flow Instrumentation of Australia, the Cobra probe is a fast-response, four-hole pressure probe that provides dynamic, three-component velocity and static pressure measurements up to a maximum speed of 107 knots (55 m/s) within an acceptance cone of ±45°. The flow magnitude (U), pitch (θ), and yaw (ψ), deduced from the measured probe-hole pressure, can be converted into three orthogonal directions of flow speed using the following equations:

$$u = U\cos(\theta)\cos(\psi), \tag{2}$$

$$v = U\cos(\theta)\sin(\psi), \tag{3}$$

$$w = U\sin(\theta). \tag{4}$$

For the computational data, flow components *u*, *v*, and *w* were obtained at the same points in space for comparison with the experimental data. For the experimental measurements for the Red 20° wind condition, a significant portion of the instantaneous flow measurements occurred beyond the 45 degree acceptance cone of the probe due to the highly turbulent nature of the airwake. Therefore, direct comparison of the measured orthogonal mean and unsteady values is not possible. By converting the computational data to U, θ, and ψ, the probability distributions of these quantities can be used for comparison instead. This analysis is discussed in Section 5.2.

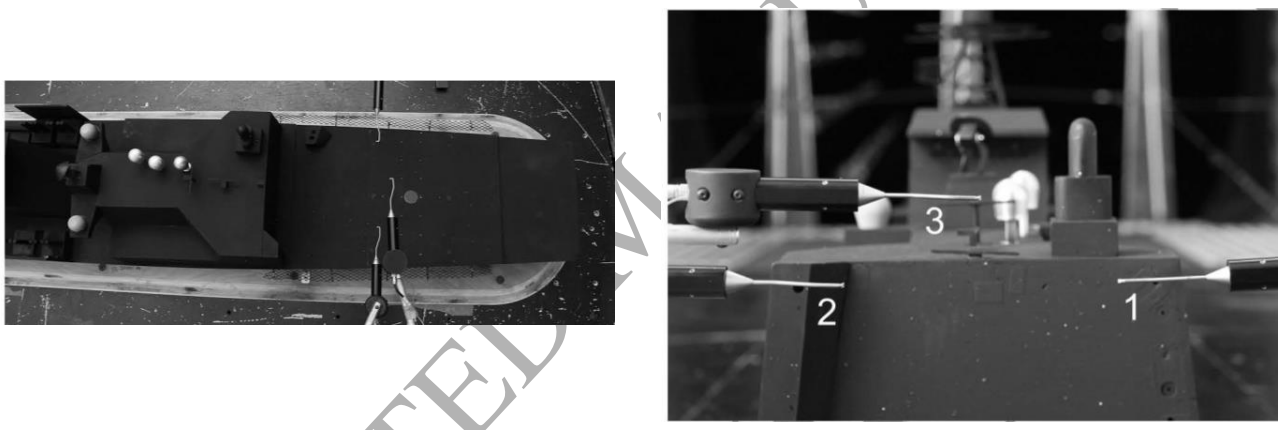

Top view Back view

Figure 16. Locations for Cobra probe airwake measurements for the CPF model in the 3 m × 6 m wind tunnel.

4.2 Particle Image Velocimetry Meassurements

During another experimental campaign with the CPF in 2012, particle image velocimetry (PIV) was used to measure the plane-wise flow characteristics in the CPF airwake. The data from this experiment have also not been previously made available in the public domain. Due to the low availability of laser light in this large wind tunnel facility, the uncertainties in the lateral flow component and unsteady flow components were too high to present here. Longitudinal (*u*) and vertical (*w*) flow components, over a

small window in the ship's airwake, have been shown to be of satisfactory quality for CFD validation. Only these results are presented in this paper.

Figure 17 illustrates the planes laid out over the CPF flight deck for the PIV measurements. All PIV data were acquired using the LaVision Stereoscopic (3D) PIV equipment and software package. PIV data were collected for 15 vertical-longitudinal planes (x-z planes in the ship coordinate system). For the sake of brevity, only five planes as shown in Figure 17 are discussed in this paper. A total of 700 image pairs were acquired at each measurement plane for each incident wind angle and tunnel speed.

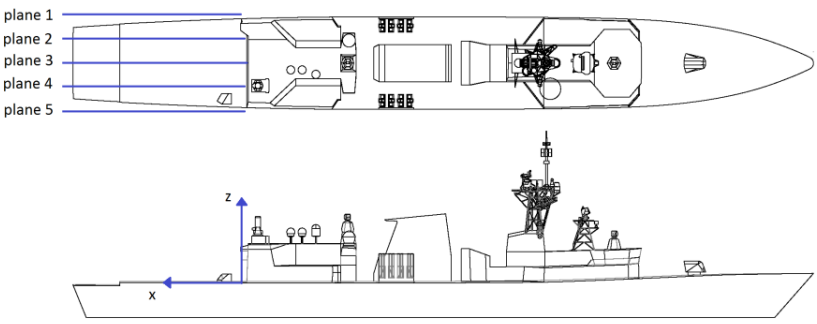

Figure 17. Layout of the PIV measurement planes located in the CPF ship airwake.

4.3 Computational Setups for the CPF

Figure 18 shows the real-world CPF geometry [33]. Zan et al. [19] carried out analysis of CPF airwakes. For their experiments, they removed most of the smaller structures on the ship including the small lattice radar-mast from the 1:50 scale model and the main mast was also simplified. In their CFD model, which was used for a steady-state simulation, the main mast was removed and the bridge shape was modified to introduce more 90° angles. In the present study, after the aforementioned successful validation of the CFD solver OpenFOAM against SFS2 geometry, OpenFOAM was applied to the CPF. The present simulations were performed in a time-accurate manner, which allows for analysis of unsteadiness and turbulence in the airwake. The models used in the current CFD study are shown in Figure 18. They were built based on

the wind tunnel model shown in Figure 17. Slight differences exist between the present CFD and 2013 wind tunnel models as the CFD model retained the angled corner at the top of the hangar on the port side (Figure 18) whereas the 2013 wind tunnel model did not (cf. flat top of hanger near probe 2 in Figure 16). Nevertheless, the present CFD and wind tunnel models included the masts and other smaller structures of the CPF. They are more representative of the actual ship geometry when compared with the models used in Ref. [19], although difficulties were encountered with meshing the complex geometry of the masts and computing the complicated flowfield past multiple bluff bodies. In addition, a CFD model without masts, shown in Figure 18b, was used to numerically evaluate the mast effects on the ship airwake, which will be discussed later in the paper.

Figure 18. A Canadian patrol frigate [33].

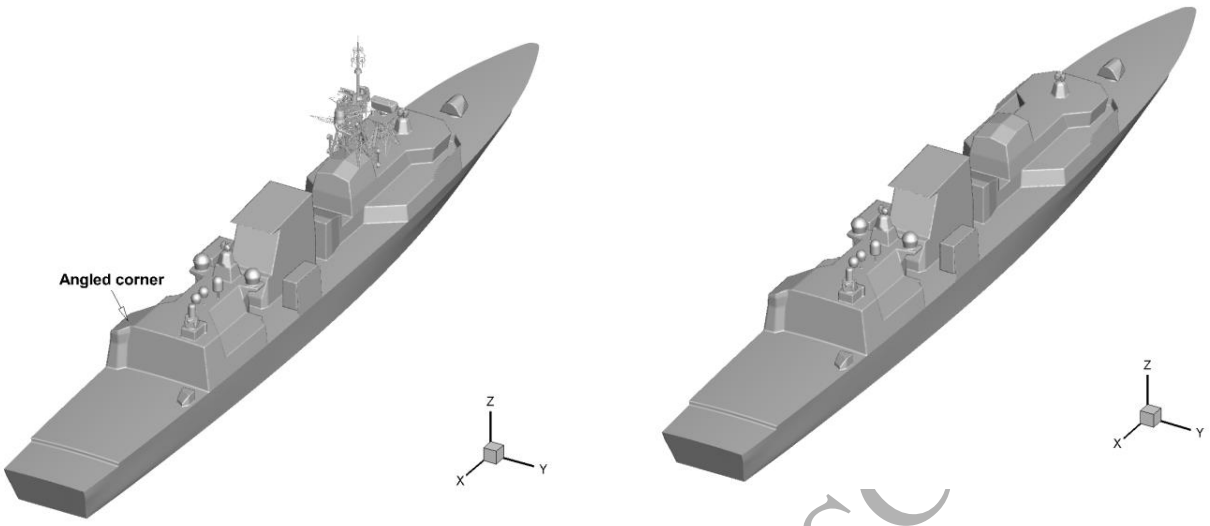

a) With masts b) No masts

Figure 18. CPF models used in the present CFD study.

The computational setups were similar to those used in the SFS2 simulations. Because the dimensions of some small structures are on the order of 3.8 mm (0.15 inches) for the full-scale CPF, the simulations were performed at full scale to keep the geometry and solution values at a reasonable magnitude that were greater than machine zero. Owing to the complexity of CPF superstructure features, unstructured grids were used near the ship, except in the airwake where a structured grid was employed, as demonstrated in Figure 19. This form of hybrid grid eased the mesh generation, which was particularly important when the masts were included. The grid spacing in the ship airwake was 10 inches at full scale, which was 20% smaller than the one used for the aforementioned SFS2 simulations and thus comparable to the spacing of the fine mesh used by Forrest and Owen [5] for the SFS2 geometry.

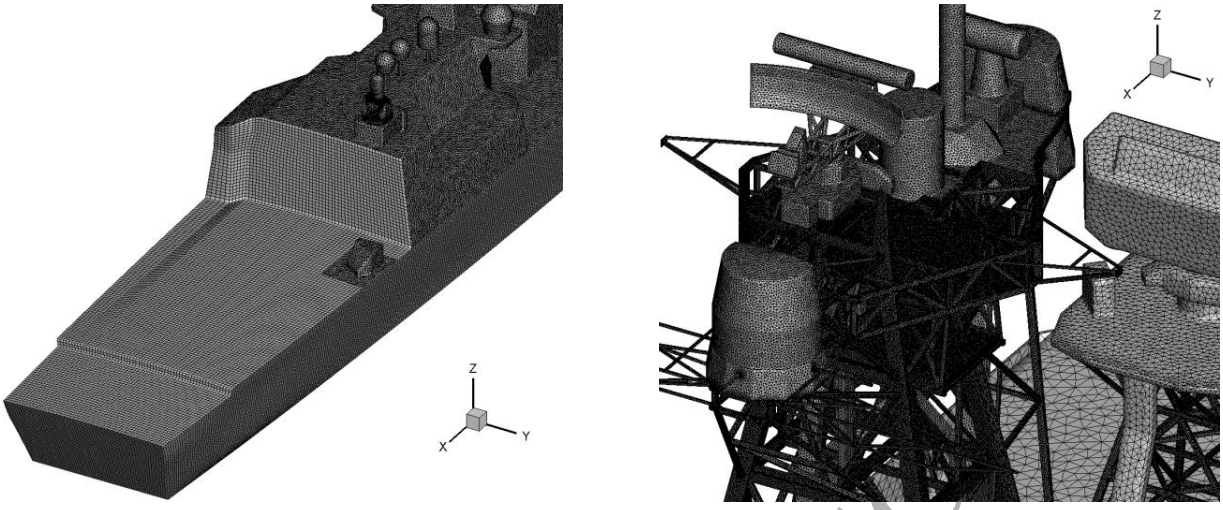

Figure 19. Surface mesh covering the CPF used in the present CFD study.

Difficulties were experienced when meshing the masts. The local spacing around the masts was determined according to the dimensions of the small structures, to ensure every small structure had at least one control cell on its surface. Polsky mentioned that small geometric features such as antennas and masts can influence the turbulent wake signature behind large naval vessels [34]. In order to evaluate the effects of the CPF masts on the ship airwake flows, two CPF configurations were used for the present CFD study – one with the original masts and the other with the masts omitted, as shown in Figure 18. As a result, the final grid consisted of 28.5 million cells for the no-mast case and 61.2 million cells for the with-mast case.

A uniform incoming flow condition was assumed, similar to a ship moving forward in low winds. The freestream velocity U_∞ was set to 20 m/s in the computations. The freestream turbulence intensity was set to 10% for the CFD simulations, which is comparable to the 9% measured in wind tunnel tests of the CPF model with the triangular spires. In this study, computations were carried out for a headwind and a Red 20° wind condition. Because of the complex multiple bluff bodies, numerical instabilities were encountered in computations when using the second-order central differencing scheme that was employed for SFS2 geometry. Instead, a linear-upwind stabilized transport (LUST) scheme was used in computations for the no-masts case and a linear upwind scheme for the with-masts case. The computations

were started from a uniform flow set as freestream. A timestep of 1×10^{-3} seconds was used in the current CFD work, which resulted in a non-dimensional timestep $CFL_{max} \sim 4$ (detected at the masts rather than in the ship airwake). The computations were performed for 60 seconds of physical time, resulting in nine units of flow through time (l_s/U_∞), with 50 seconds used for final sampling.

5 CPF Results and Discussion

Pointwise validation of CFD results was conducted for headwind (section 5.1) and Red 20° wind (section 5.2) using the Cobra Probe data described in section 4.1 and plane-wise mean flow validation was conducted (section 5.3) using the PIV data described in section 4.2. All results are shown using values that are normalized relative to the reference wind tunnel speed, U_∞. In this paper, the overbar notation refers to a mean of the quantity, and the prime notation refers to the standard deviation of a quantity.

5.1 Headwind

In Table 1 to Table 3 and Figure 20, the computed results are compared with the experimental data for the CPF model with a headwind. The experimental data have been scaled using the reduced frequency to match the full-scale conditions. In general, the CFD predicted the velocities qualitatively. However, quantitative discrepancies were observed. In particular, the present CFD simulations under-predicted the mean velocity at the starboard and mid-point for the no-masts and with-masts cases, respectively. The computed velocity fluctuations and the integrated turbulence intensities were comparable to the experimental data. The computed power spectra decayed somewhat faster when compared with the experiments. It is interesting that the omission of the masts was able to deliver satisfactory numerical accuracy for the wake flow. The no-masts case showed even slightly better results than the with-masts case, since the LUST scheme was applied to the no-masts case while the linear-upwind scheme was employed for the with-masts case. LUST is an interpolation scheme in which linear-upwind is blended with linear interpolation to stabilise solutions while maintaining second-order behavior. The present

version of OpenFOAM uses a fixed blended scheme with 0.25 linear-upwind and 0.75 linear weights, which was unable to maintain the numerical stability when applied to the with-masts case. Enabling flexible blending of the linear-upwind and linear weights may provide a way to improve the numerical accuracy for the with-masts case. Nevertheless, the airwake results from the no-masts case are promising for parametric studies on ship airwakes as the computational cost for the with-masts case is more than twice as high. The effect of the inclusion of masts will be discussed further later.

Table 1 Mean velocities ($\bar{u}/U_\infty, \bar{v}/U_\infty, \bar{w}/U_\infty$) in the CPF flight deck wake at headwind

Probes	1 (Starboard)			2 (Port)			3 (Mid)		
	$\bar{u}/U_\infty$	$\bar{v}/U_\infty$	$\bar{w}/U_\infty$	$\bar{u}/U_\infty$	$\bar{v}/U_\infty$	$\bar{w}/U_\infty$	$\bar{u}/U_\infty$	$\bar{v}/U_\infty$	$\bar{w}/U_\infty$
Experimental	0.48	-0.07	-0.14	0.69	0.08	-0.18	0.73	0.02	-0.13
CFD, no masts	0.41	-0.01	-0.10	0.59	0.02	-0.12	0.75	0.01	-0.14
CFD, with masts	0.46	-0.01	-0.11	0.61	0.05	-0.10	0.56	0.01	-0.10

Table 2 Velocity fluctuations (u'/U_∞, v'/U_∞, w'/U_∞) in the CPF flight deck wake at headwind

Probes	1 (Starboard)			2 (Port)			3 (Mid)		
	u'/U_∞	v'/U_∞	w'/U_∞	u'/U_∞	v'/U_∞	w'/U_∞	u'/U_∞	v'/U_∞	w'/U_∞
Experimental	0.12	0.16	0.16	0.14	0.12	0.10	0.14	0.13	0.10
CFD, no masts	0.14	0.13	0.10	0.15	0.10	0.09	0.09	0.09	0.07
CFD, with masts	0.14	0.13	0.10	0.18	0.13	0.13	0.09	0.10	0.09

Table 3 Turbulence intensity ($\sqrt{(u'^2+v'^2+w'^2)/3}/U_\infty$) in the CPF flight deck wake at headwind

Probes	1 (Starboard)	2 (Port)	3 (Mid)
Experimental	0.14	0.14	0.14
CFD, no masts	0.13	0.12	0.08
CFD, with masts	0.12	0.15	0.09

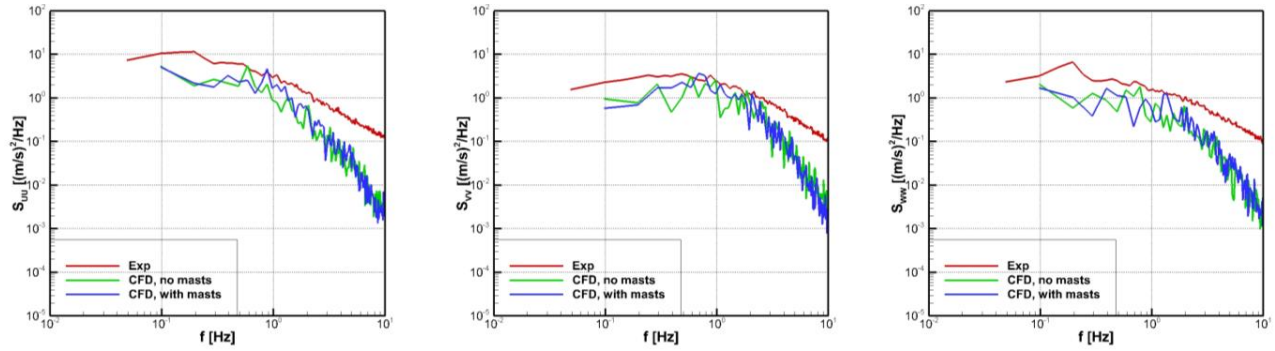

Point 1: Starboard

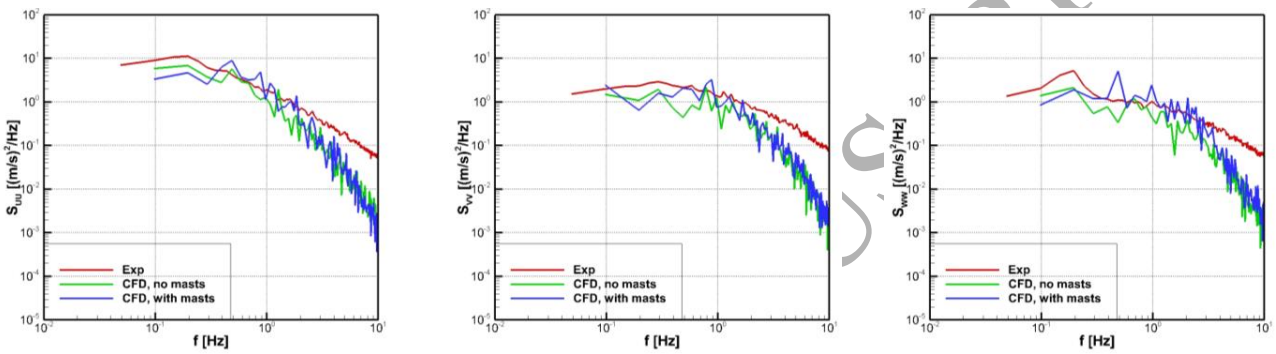

Point 2: Port

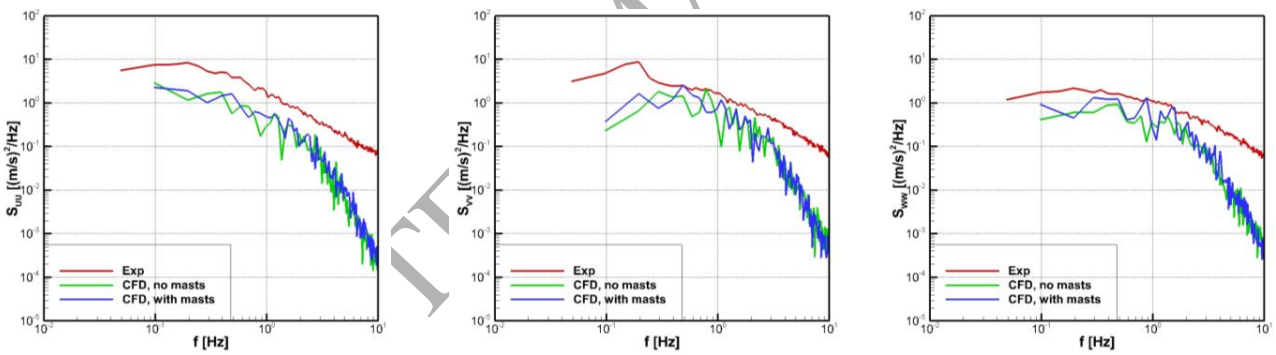

Point 3: Mid

Figure 20. Power spectral density plots for the CPF at headwind.

5.2 Red 20° Wind

As discussed in Section 4.1, experimental measurements of the wake flow were acquired with a single Cobra probe. In the airwake of the CPF at Red 20° wind condition, a significant percentage of the instantaneous flow measurements extended beyond the ±45° acceptance cone of the probe. Therefore, an additional post-processing procedure was needed for validation. The probability distributions of the quantities flow magnitude, pitch, and yaw, as shown in Figure 21, illustrate the clipping in the experimental measurements caused by the ±45° acceptance cone. The flow measurements beyond the ±45° acceptance cone showed artificial zero values and therefore gathered on the horizontal coordinate axis line in Figure 21, e.g., for negative pitch angles for the starboard point.

Figure 21 also shows the same calculated distributions for the computed results with (blue) and without (green) masts. A qualitative examination of these results reveals good agreement between the experimental and numerical data sets. The starboard point and the mid-point show somewhat better agreement for the case without masts while the port side shows equivalent agreement.

To obtain a quantitative comparison between experimental and computational data, the experimental data were curve-fitted with a normal distribution. Although the true distributions are not universally normal, examination of the fits in Figure 22 shows that the peak and width (mean and standard deviation, respectively) are well represented by the curve fits. Tables 4 and 5 show the fitted mean and standard deviation for the experimental results of flow magnitude, pitch, and yaw presented along with the same quantities calculated directly from the computational results.

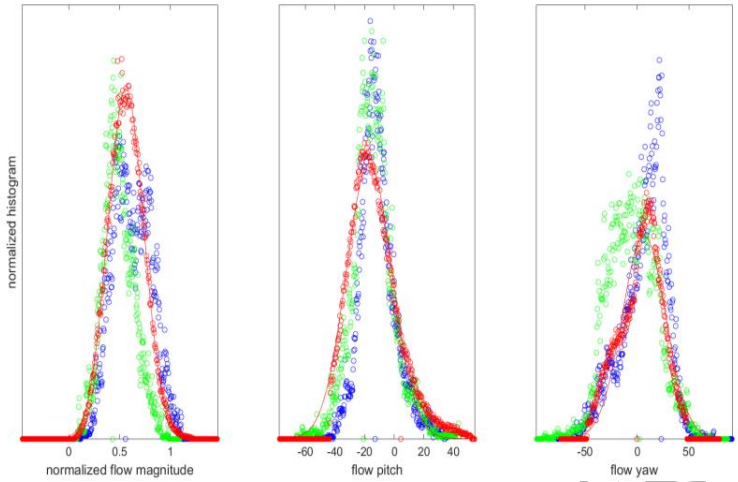

Point 1: Starboard

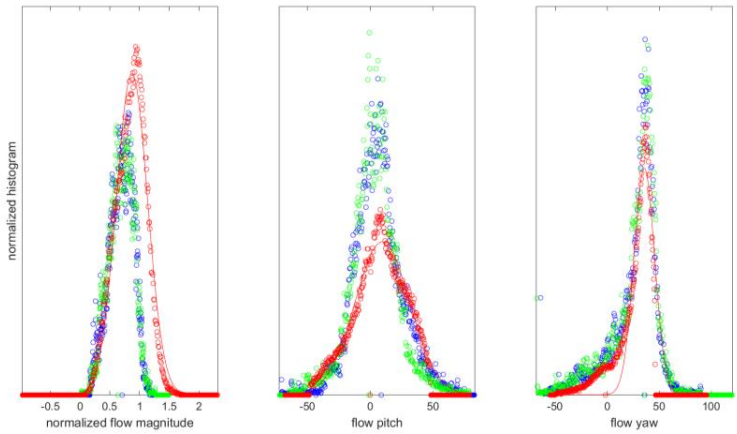

Point 2: Port

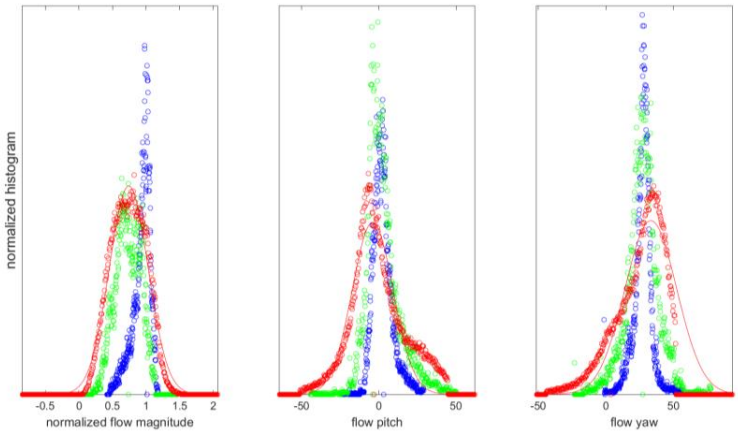

Point 3: Mid

Figure 21. Distribution-based comparison for CPF airwake data at Red 20° wind; red – experiments, blue – CFD with masts, green – CFD without masts.

In examining Table 4, Table 5, and Figure 22, the following observations are revealed. Similar to the headwind cases, the CFD predicted the trends of the velocity distributions qualitatively. Again, the airwake results from the no-masts case are promising or even better than those from the with-masts case when compared with the experimental data.

Table 4 Mean velocity magnitude (U/U_∞), pitch θ[°], and yaw ψ[°] in the CPF flight deck wake at Red 20° wind condition

Probes	1 (Starboard)			2 (Port)			3 (Mid)		
	U/U_∞	θ[°]	ψ[°]	U/U_∞	θ[°]	ψ[°]	U/U_∞	θ[°]	ψ[°]
Experimental	0.56	-16.93	6.70	0.87	9.67	35.55	0.74	-4.02	33.35
CFD, no masts	0.49	-14.16	-4.65	0.69	3.23	26.04	0.73	2.98	27.27
CFD, with masts	0.62	-11.27	7.43	0.69	6.21	26.19	0.93	2.65	27.48

Table 5 Fluctuations of velocity (U'/U_∞), pitch θ'[°], and yaw ψ'[°] in the CPF flight deck wake at Red 20° wind condition

Probes	1 (Starboard)			2 (Port)			3 (Mid)		
	U'/U_∞	θ'[°]	ψ'[°]	U'/U_∞	θ'[°]	ψ'[°]	U'/U_∞	θ'[°]	ψ'[°]
Experimental	0.17	15.49	none*	0.26	21.77	none*	0.29	13.28	19.20
CFD, no masts	0.15	14.55	23.01	0.20	18.91	23.51	0.18	11.82	12.66
CFD, with masts	0.18	11.96	21.04	0.20	19.25	22.60	0.13	6.62	7.17

*Normal distribution fit deemed by inspection not to appropriately represent the velocity fluctuations of the original signal.

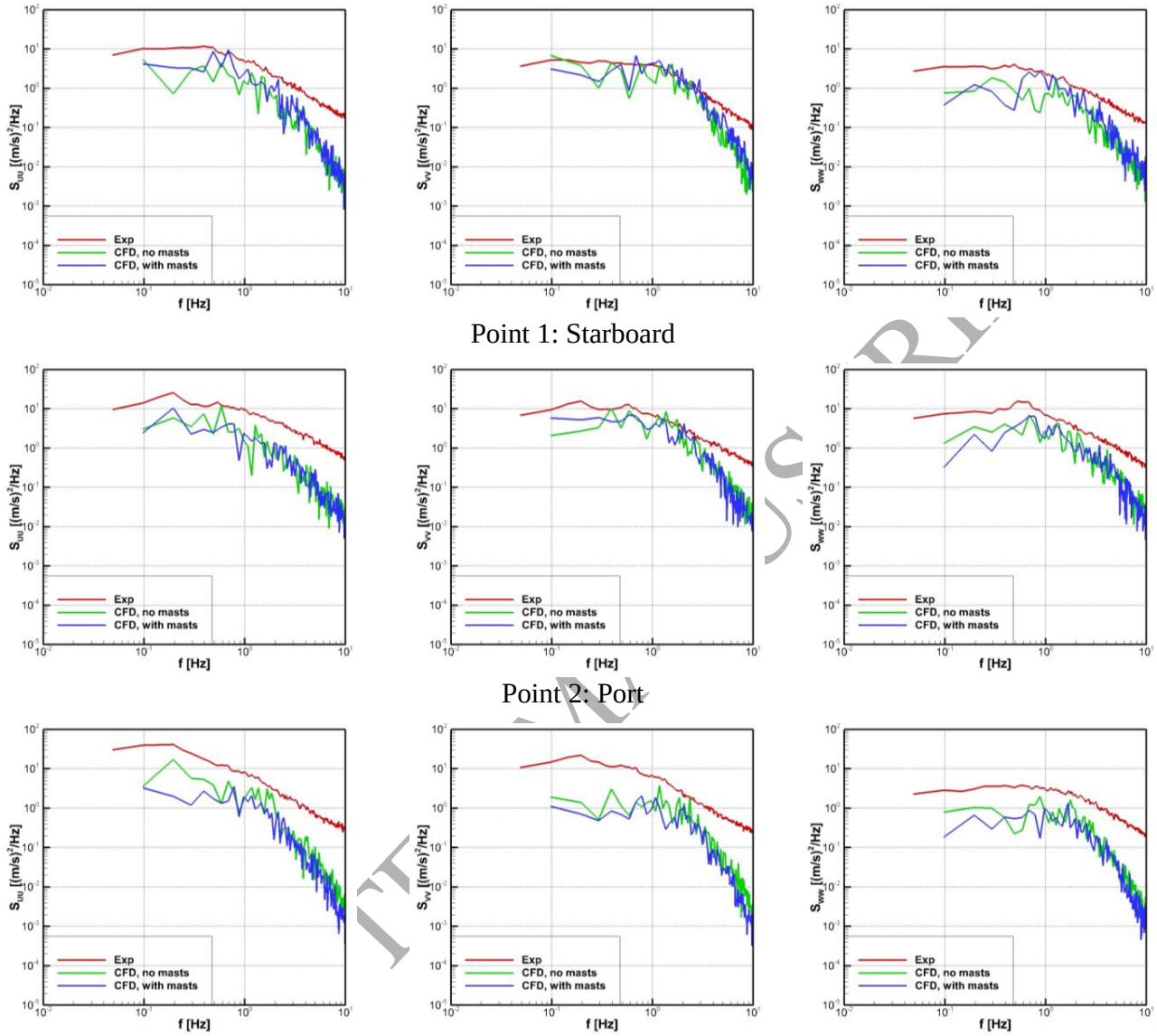

Figure 22. Power spectral density plots for the CPF at Red 20° wind.

5.3 Velocity Data Supplied to Flight Simulator

For CFD validation purposes, PIV measurements were performed on selected planes in the ship airwake, as discussed in section 4.2.

The unsteady CFD simulations produced large quantities of time-varying data for airwake velocities in three dimensions. The CFD simulations were performed for a grid spacing of 10 inches at the ship

airwake for the full-scale CPF. In order to reduce the excessive data storage requirements and ensure the CFD data are suitable for direct implementation into a real-time simulation environment, a coarser structured output grid was designed to cover the wake region of the CPF, where helicopters are expected to operate, as shown in Figure 23. A structured output grid was generated with a uniform spacing of one meter for a rectangular box with *x* from 4 to 28 m, *y* from -10 to 10 m, and *z* from 1 to 12 m. The origin of the coordinates was located at the centre of the deck where the hangar meets the deck. When the output grid did not match the CFD grid, Forrest et al. [3] and Hodge et al. [8] used interpolation to map the data from the CFD mesh to the output grid. However, since interpolation may smear some of the unsteadiness of the flow, the nearest points from the CFD mesh were selected to represent the desired output locations in this study. This way, the maximum bias in distance was limited by the grid resolution, namely 10 inches. The sampling data on the output grid were then stored in a look-up table and supplied to a flight simulation facility at Defence Research and Development Canada **(**DRDC**).** The flight simulator may use interpolations depending on its own algorithm. However, its interpolation may have smearing effect too, the same as that in mapping CFD data to the output grid, which needs to be carefully addressed.

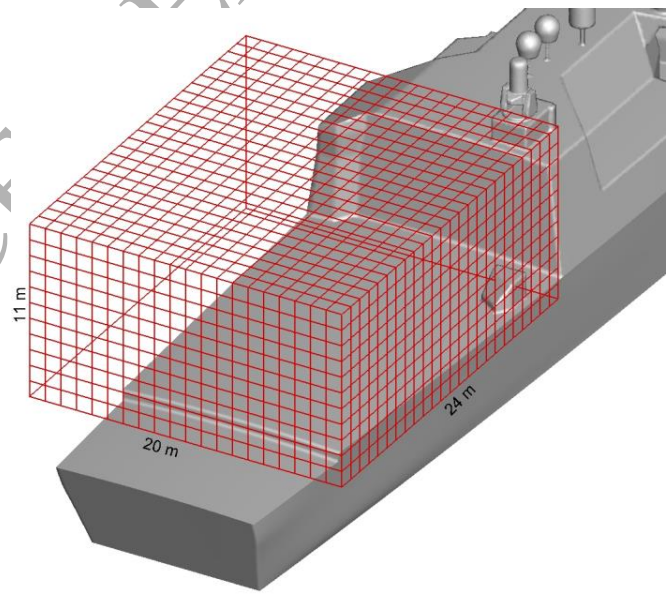

Figure 23. CPF output grid for the flight simulator look-up tables.

To validate the data, the computed output grid results sampled during the CFD simulations were compared with the PIV results. Figure 24 and Figure 25 compare the flowfield with headwind for the planes in the ship airwake, as illustrated in Figure 17. When compared with the PIV results, the computed results capture the major features of the flow. For the headwind case, a reduction in longitudinal velocity can be seen near the centre, within the wake behind the hangar. Significant gradients exist in the time-averaged values of the velocity components, which would affect the trim of the helicopter. The CFD predicted separation zone was slightly smaller than what is that shown in the PIV results. The results from both CFD configurations with and without the masts are reasonably comparable. Figure 26 and Figure 27 compare the flowfield between the experimental and CFD results with Red 20° wind. This test case is much more challenging. As for the headwind case, the CFD predicted separation zone was slightly smaller when compared with the PIV results. However, in general the CFD is in good agreement with the PIV results and the velocity deficit and gradients are reasonably well predicted. The prediction of the separation zone using the no-masts configuration was even better than that using the with-masts case. This was mainly attributed to the applied numerical scheme.

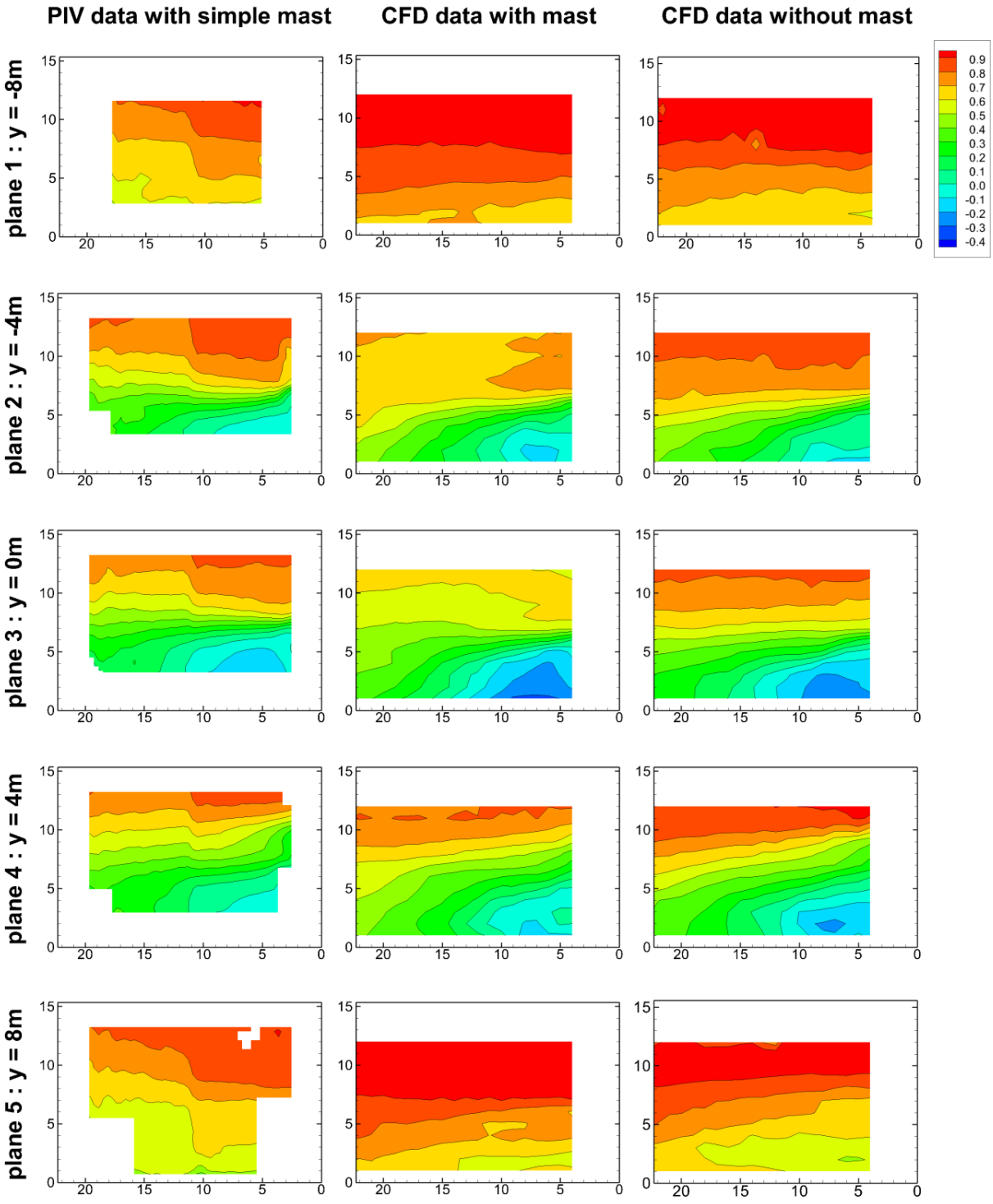

Figure 24. CPF airwake data, headwind, streamwise mean flow, dimensions in meters.

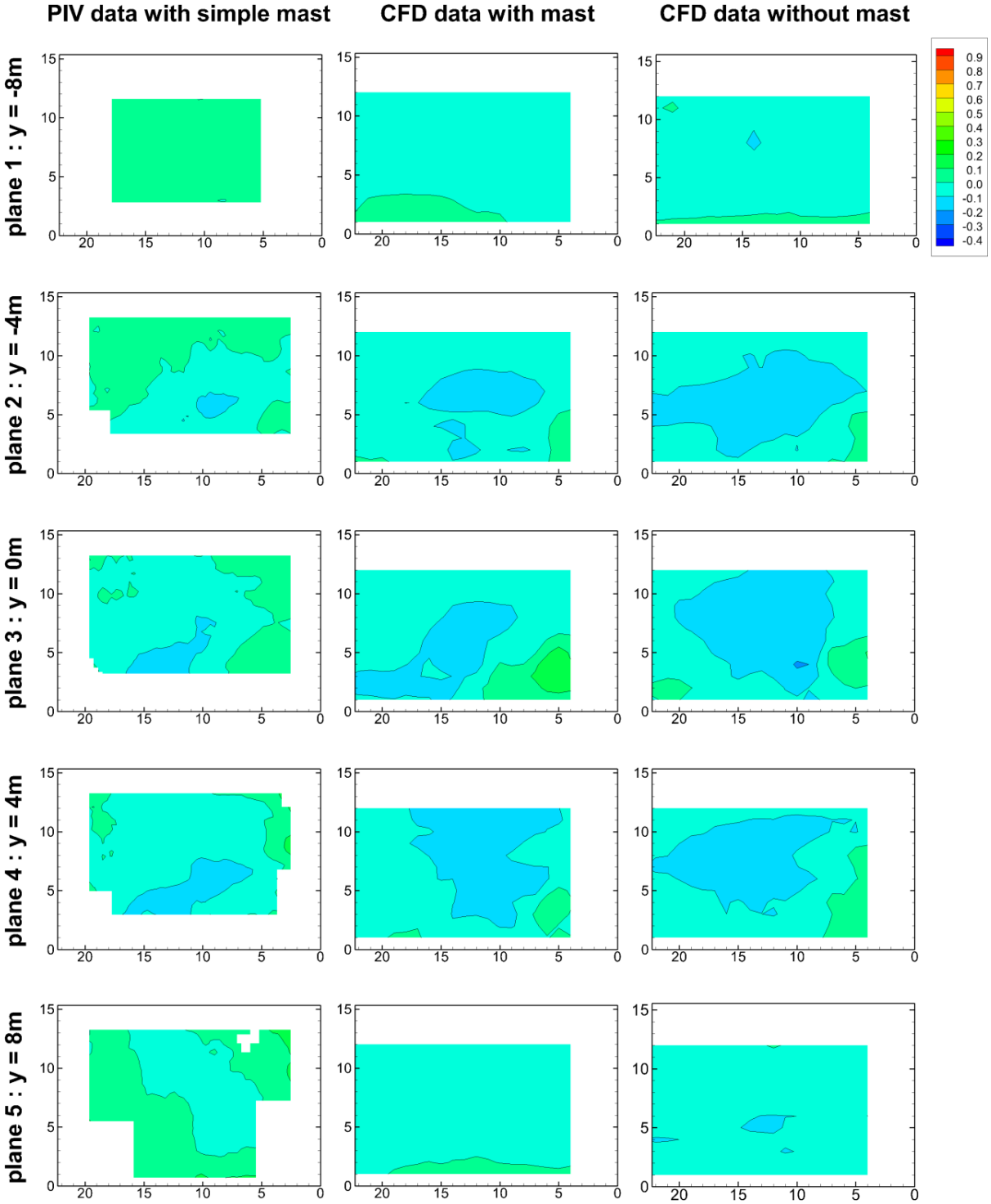

Figure 25. CPF airwake data, headwind, vertical mean flow, dimensions in meters.

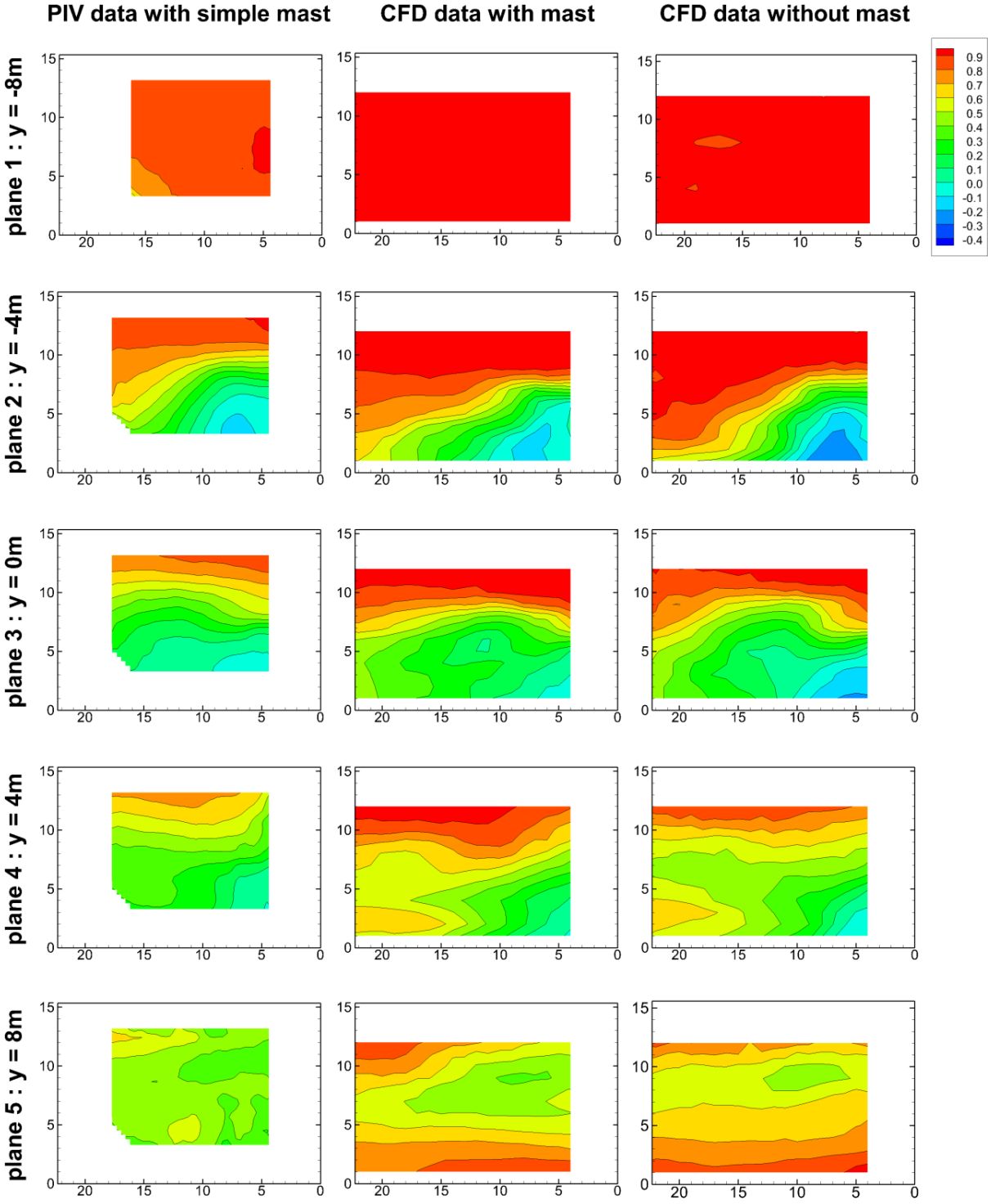

Figure 26. CPF airwake data, Red 20° wind, streamwise mean flow, dimensions in meters.

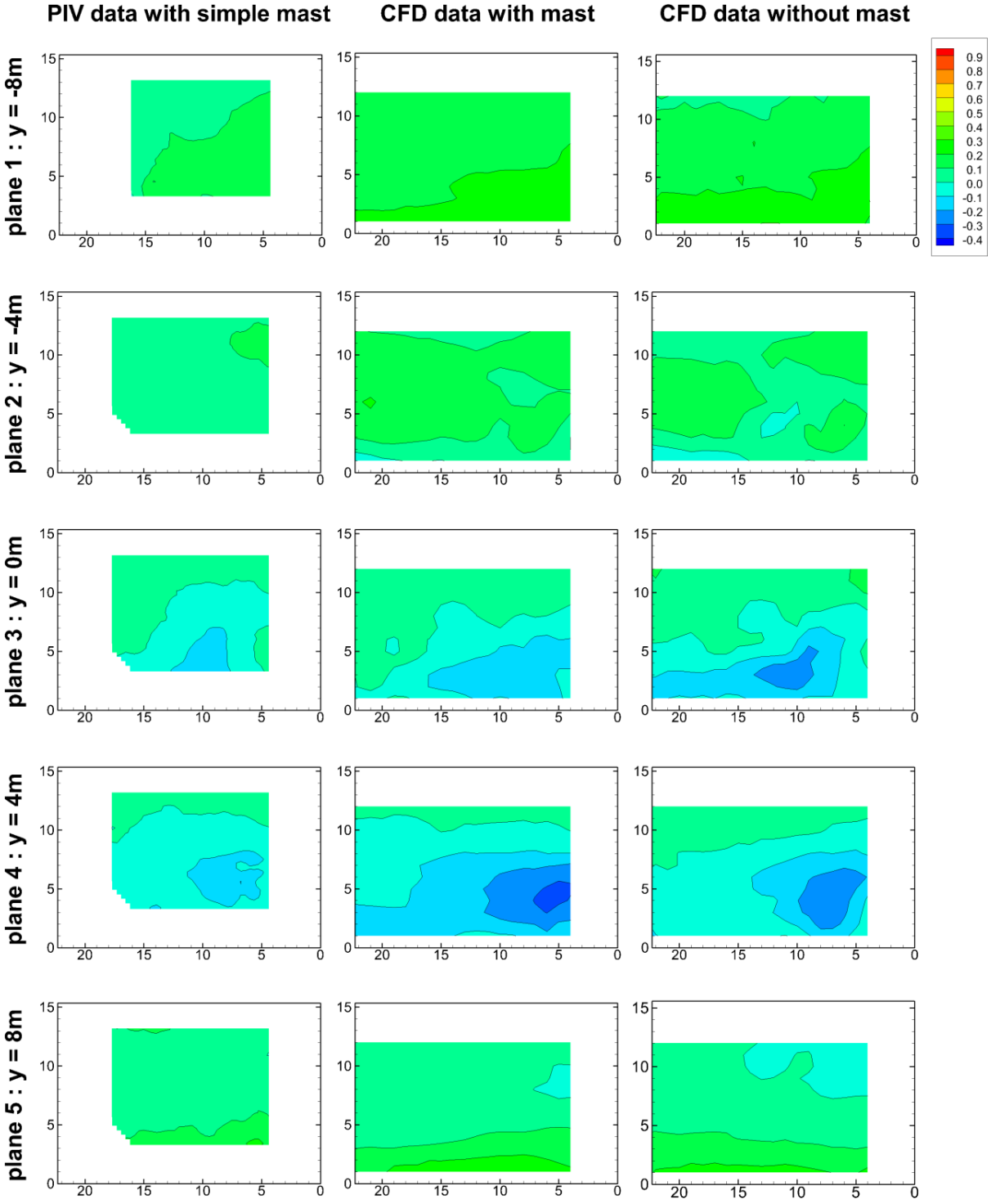

Figure 27. CPF airwake data, Red 20° wind, vertical mean flow, dimensions in meters.

5.4 Masts Effect

As mentioned earlier, numerical instability was encountered for the with-masts case when using the LUST scheme. The LUST scheme blends linear-upwind with linear interpolation to stabilize solutions while maintaining second-order behavior. As a result of the instability, the LUST scheme was applied to the no-masts case while the linear-upwind scheme was employed for the with-masts case. To confirm the influence of the numerical schemes, computations using the linear-upwind scheme were also performed for the no-masts configuration. Table 6 compares the results obtained using the two numerical schemes for the no-masts configuration with Red 20° wind. The mean velocity using the linear-upwind scheme showed obvious discrepancies from the experimental data when compared with the LUST scheme and this is expected. On the other hand, the calculated probability distributions for the computed CPF airwake results using the linear-upwind scheme for the no-masts case (not shown) were nearly identical to those of the linear-upwind results for the with-masts case (blue in Figure 21) rather than the LUST results for the no-masts cases (green in Figure 21), indicating that the numerical scheme played a primary role in this study. Mathematically speaking, incompressible or subsonic flows are mainly elliptic. Linear (central) interpolation considers the elliptic behavior while upwind schemes do not. The present version of OpenFOAM uses a fixed blended scheme with 0.25 linear-upwind and 0.75 linear weights. It is believed that enabling flexible blending of the linear-upwind and linear weights will improve the numerical accuracy for the with-masts case.

Table 6 Mean velocity magnitude (U/U_∞), pitch θ[°], and yaw ψ[°] in airwake of the no-masts CPF wake with Red 20° wind

Approaches	1 (Starboard)			2 (Port)			3 (Mid)		
	U/U_∞	θ[°]	ψ[°]	U/U_∞	θ[°]	ψ[°]	U/U_∞	θ[°]	ψ[°]
Experimental	0.56	-16.93	6.70	0.87	9.67	35.55	0.74	-4.02	33.35
LUST	0.49	-14.16	-4.65	0.69	3.23	26.04	0.73	2.98	27.27
Linear-upwind	0.70	-13.00	14.09	0.66	7.96	26.79	1.02	1.83	25.71

As pointed out by Polsky [34], small geometric features such as antennae and masts can influence the turbulent wake signature behind large naval vessels. However, only the flowfield right behind an antenna model was investigated in that work and the effect on the ship airwake was inconclusive. In this present study, numerical results from the linear-upwind simulations were compared for both configurations with and without masts. A closer look at the results listed in Table 4 and Table 6 shows that for both the with- and no-masts configurations using the linear-upwind scheme, the computations over-predict the mean velocity at the starboard and mid-point. However, in general, the results of the with-masts configuration are closer to the experimental data. This comparison numerically confirms the effects of the masts. On the other hand, omitting relatively small structures like masts may improve the numerical stability, and thus could allow the application of more accurate numerical schemes as a trade off. Nevertheless, validation against at-sea and wind tunnel tests is the only way to check the adequacy appropriateness or impact of omission, depending on the focus of interest. In any case, combined computational and experimental simulations provide a reliable means for ship airwake investigations.

While quantitative differences in airwake results are the focus of this study, any differences small enough not to affect helicopter operations can be practically neglected. Unpublished studies with and without masts using the technology described in McTavish et al. [35] indicate the CPF masts have a negligible effect on helicopter operations.

6 Concluding Remarks

The open-source OpenFOAM was validated for computations of three-dimensional unsteady incompressible ship airwake flows behind a simple frigate shape and the real CPF. Applying the Spalart-Allmaras DDES to model the turbulence, the computed results showed reasonable agreement with the

wind tunnel data, demonstrating the ability of OpenFOAM and the DDES model to capture important features in unsteady ship airwake flows.

Combined computational and experimental simulations provide a reliable means for ship airwake investigations. The computational and experimental simulations showed the typical reduction in velocity within the wake behind the hangar and significant gradients in the velocity components, which are known to affect helicopter operations. The frequency content and power of the unsteady airwake flows for full scale are the same as for model scale, confirming numerically the insensitivity of the flow to Reynolds number for the bluff-body geometries investigated in this study.

The numerical simulations also provided additional insights into the effects of the masts. Based on experimental measurements of rotor loads, the masts appear to have a negligible effect on helicopter operations. This observation motivated the removal of the masts in numerical simulations when the focus of interest is on ship airwakes. The present numerical study showed that removing the masts in numerical simulations may permit the use of more accurate numerical schemes and reduce the computational time as the complex flow around the masts is more likely to cause numerical instabilities. This effect is worthy of further investigation and must be carefully validated against at-sea and wind tunnel tests.

Despite significant progress made in CFD capability development, there are still a number of technical challenges towards real-time applications in flight simulators in Canada. From the aerodynamic point of view, ship motion effects on the ship airwake are being investigated as it could possibly play an important part when large amplitude ship motions are present. Secondly, the effect of atmospheric turbulence and atmospheric boundary layer on the ship airwake need to be verified. Then the challenge would be coupling or integration with other technical parts in a flight simulator, particularly the rotor model. This has to be done by working together with other technical experts, simulator manufacturers, and qualified flight test pilots. Although the CFD simulations performed to generate real environment

flowfield data is the same as or similar to CFD validation practices against a wind tunnel experiment, for integration into the flight simulator, there are also a number of technical questions which remain open on the data export to the simulator, including time range, sampling rate, and wind velocity intervals. CFD simulations can generate data of terabytes for a single test case, which requires huge storage. How to extract and output data to the flight simulator to make it effectively work will be a future technical challenge. In Canada, these developments are ongoing, following from the technical progress demonstrated in this paper.

7 Acknowledgments

The present work was partially funded by the Defence Research and Development Canada (DRDC), Director General Aerospace Equipment Program Management (DGAEPM) of Canada, and the Air Defense System (ADS) program of NRC. Dr. Chris Sideroff from the Applied CCM Canada provided technical support for the grid generation of the CPF. Special thanks are also given to Dr. Stuart McIlwain from NRC, for his fruitful discussions regarding the results interpretation and presentation.

References

[1] Polsky, S. NAVAIR Airwake Modeling & More, *HPC User Group Forum*, 2008.

[2] Polsky, S. Progress towards Modeling Ship/Aircraft Dynamic Interface, *HPCMP Users Group Conference, IEEE Computer Society*, 2006.

[3] Forrest, J., Owen, I., Padfield, G., and Hodge, S. Ship–Helicopter Operating Limits Prediction Using Piloted Flight Simulation and Time-Accurate Airwakes. *Journal of Aircraft*, Vol. 49, No. 4, pp 1020-1031, 2012.

[4] Polsky, S. and Wilkinson, C. A Computational Study of Outwash for a Helicopter Operating near a Vertical Face with Comparison to Experimental Data. *AIAA Modeling and Simulation Technologies Conference*, Chicago, Illinois, AIAA 2009-5684, August 10-13, 2009.

[5] Forrest, J, and Owen, I. An Investigation of Ship Airwakes using Detached-Eddy Simulation. *Computers & Fluids*, Vol. 39, pp 656–673, 2010.

[6] Polsky, S. Computational Study of Unsteady Ship Wake. *AIAA Aerospace Sciences Meeting, Reno Nevada*, AIAA-2002-1022, January 14-17, 2002.

[7] Polsky, S., Imber, R., Czerwiec, R. and Ghee, T. A Computational and Experimental Determination of the Air Flow around the Landing Deck of a US Navy Destroyer (DDG): Part II. *AIAA Applied Aerodynamics Conference*, Miami, FL, AIAA-2007-4484, June 25-28, 2007.

[8] Hodge, S., Forrest, J., Padfield, G., and Owen, I. Simulating the Environment at the Helicopter-ship Dynamic Interface: Research, Development and Application. *The Aeronautical Journal*, Vol. 116, No. 1185, pp 1155-1184, 2012.

[9] Wilkinson, C.H., Zan, S.J., Gilbert, N.E., and Funk, J.D. Modeling and Simulation of Ship Air Wakes for Helicopter Operations – A Collaborative Venture, *Symposium on Fluid Dynamics Problems of Vehicles Operating near or in the Air-Sea Interface*, Amsterdam, Netherlands, October. NATO RTO-MP-15, pp 8-1 to 8-12, 1998.

[10] Zan, S. On Aerodynamic Modelling and Simulation of the Dynamic Interface. *Proc Inst Mech Eng, Part G: J Aerospace Eng*, Vol. 219, No. 5, pp 393–410, 2005.

[11] Syms, G. Simulation of Simplified-frigate Airwakes using a Lattice-Boltzmann Method. *J Wind Eng Ind Aerodynamics*, Vol. 96, No. 6-7, pp 1197–1206, 2008.

[12] Zhang, F., Xu, H., and Ball, N. Numerical Simulation of Unsteady Flow over SFS 2 Ship Model. *47th AIAA Aerospace Sciences Meeting Including the New Horizons Forum and Aerospace Exposition*, Orlando, Florida, AIAA 2009-81, 5-8 January, 2009.

[13] Spalart P. R., and Allmaras S. R. A One-Equation Turbulence Model for Aerodynamic Flows. *30th Aerospace Sciences Meeting and Exhibit*, AIAA 1992-0439, 1992.

[14] Zhang, F., and Su, J. Numerical Investigation of the Interaction of the Airwake of an SFS 2 Ship with the Downwash of a Bell 412 Helicopter, *CASI AERO*, 26-28 April., 2011.

[15] Menter F, Kuntz M, and Langtry R. Ten years of industrial experience with the SST turbulence model. In: Hanjalic K, Nagano Y, Tummers M, editors. Turbulence, Heat and Mass Transfer, vol. 4. Redding (CT): Begell House; pp 625–32, 2003.

[16] Rajmohan, N., Zhao, J., He, C., Polsky, S. Development of a Reduced Order Model to Study Rotor/Ship Aerodynamic Interaction. *AIAA Modeling and Simulation Technologies Conference*, Kissimmee, Florida, AIAA-2015-0907, January 5-9, 2015.

[17] Jasak, H., Jemcov, A., and Tukovic, Z. OpenFOAM: A C++ Library for Complex Physics Simulations. *International Workshop on Coupled Methods in Numerical Dynamics*, Dubrovnik, Croatia, September 19, 2007.

[18] Spalart, P. R., Jou, W. H., Strelets, M., and Allmaras, S. R.. Comments on the Feasibility of LES for Wings, and on a Hybrid RANS/LES Approach. *Advances in DNS/LES*, Greyden, pp 137–147, 1997.

[19] Zan, S, Syms, G, Cheney, B. Analysis of Patrol Frigate Air Wakes. *NATO RTO-AVT Symposium on Fluid Dynamics Problems of Vehicles Operating near or in the Air-Sea Interface*, Amsterdam, The Netherland, 5-8 October 1998.

[20] Launder, B.E., and Spalding, D.B. The Numerical Computation of Turbulent Flows. *Computational Methods: Applied Mechanical Engineering*, Vol. 3, pp 269-289, 1974.

[21] Healey, J., Establishing a Database for Flight in the Wakes of Structures. *Journal of Aircraft*, Vol. 29, No. 04, pp. 559-564, 1992.

[22] Yuan, W., Sandhu, R., Matos Jr, O., and Poirel, D. Methodology Development for Coupled Aeroelastic Analysis of Wing Flutter. *54th AIAA Aerospace Sciences Meeting*, San Diego, California, USA, 4-8 January, AIAA 2016-1550, 2016.

[23] Yuan, W., Wall, A., and Lee, R. Simulations of Unsteady Airwakes behind Ships in Motion. *31st Congress of the International Council of the Aeronautical Sciences*, Belo Horizonte, Brazil, 09-14 September, 2018.

[24] Yuan, W., Lee, R., and Wall, A. Simulation of Unsteady Ship Airwakes using OpenFOAM. *30th Congress of the International Council of the Aeronautical Sciences*, Daejeon, Korea, 25-30 September, 2016.

[25] http://www.nrc-cnrc.gc.ca/eng/solutions/facilities/wind_tunnel/2x3_metre.html.

[26] OpenFOAM. The Open Source CFD Toolbox. *User Guide*, Version 2.3.0, Feb. 2014.

[27] Spalart, P. R., Deck, S., Shur, M. L., Squires, K. D., Strelets, M. K., and Travin, A. A New Version of Detached-eddy Simulation, Resistant to Ambiguous Grid Densities. *Theoretical and Computational Fluid Dynamics*, Vol. 20, No. 3, pp 181-195, 2006.

[28] Zan, S. Technical Comment on "Computational-Fluid-Dynamics Based Advanced Ship-Airwake Database for Helicopter Flight Simulation". *AIAA Journal of Aircraft*, Vol. 40, No. 5, pp 1007, 2003.

[29] McRuer, D. T. Interdisciplinary Interactions and Dynamic Systems Integration. *International Journal of Control*, Vol. 59, pp 3–12, 1994.

[30] Yuan, W, Poirel, D, Wang, B, and Benaissa, A. Effect of Freestream Turbulence on Airfoil Limit-Cycle Oscillations at Transitional Reynolds Numbers. *AIAA Journal of Aircraft*, Vol. 52, No. 4, pp 1214-1225, 2015.

[31] http://www.nrc-cnrc.gc.ca/eng/solutions/facilities/wind_tunnel/3x6_metre.html.

[32] NATO. *Standardized Wave and Wind Environments and Shipboard Reporting of Sea Conditions*. No. STANAG 4194, Ed. 2, NATO, 1993.

[33] https://en.wikipedia.org/wiki/Halifax-class_frigate.

[34] Polsky, S. Application and Verification of Sub-Grid Scale Boundary Conditions for the Prediction of Antenna Wake Flowfields. *5th International Colloquium on Bluff Body Aerodynamics and applications*, Ottawa, Canada, July 11-15, 2004.

[35] McTavish, S., Wall, A., Lee, R. A Methodology to Correlate Simulated Airwake Data and Unsteady Helicopter Load Measurements to Shipboard Helicopter Flight Test Data. *14th International Conference on Wind Engineering*, Porto Alegre, Brazil, June 21-26, 2015.